GSA Bulletin; *https://doi.org/10.1130/B32029.1; 17 figures; 3 tables*

Seismically-enhanced hydrothermal plume advection through the process zone of the Compione extensional Fault, Northern Apennines, Italy

Alessio Lucca[1], Fabrizio Storti[1], Giancarlo Molli[1,2], Philippe Muchez[3], Andrea Schito[4], Andrea Artoni[5], Fabrizio Balsamo[1], Sveva Corrado[4], and Emma Salvioli Mariani[5]

[1]*Department of Chemistry, Life Sciences and Environmental Sustainability, Natural and Experimental Tectonics research group, University of Parma, I-43124 Parma, Italy*

[2]*Department of Earth Sciences, University of Pisa, via S. Maria, 53, I-56126 Pisa, Italy*

[3]*Katholieke Universiteit Leuven, Department of Earth and Environmental Sciences, Celestijnenlaan 200E, B-3001 Heverlee, Belgium*

[4]*Department of Sciences, Geology Section, Roma Tre University, L.go S. Leonardo Murialdo 1, I-00146, Roma, Italy*

[5]*Department of Chemistry, Life Sciences and Environmental Sustainability, University of Parma, I-43124 Parma, Italy*

*Corresponding Author Details

E-mail: alessio.lucca@studenti.unipr.it

Telephone number: +39 393 1323420

ABSTRACT

Reconstructing the paleofluid evolution in mature fault zones, which typically have complex structural architectures, is a challenging task because re-activation of pre-existing deformation structures and dissolution-reprecipitation processes are very abundant. Understanding why specific structural elements are preferentially mineralized and what are the factors leading to rapid fluid migration and accumulation, bears geological and economic implications, especially in seismically active fault zones. We studied the Compione Fault on the Tyrrhenian Sea side of the Northern Apennines orogenic wedge, Italy, which is a segment of the 30 km long Northern Lunigiana high-angle extensional fault system still active today.

The Compione Fault propagated from the metamorphic basement and accumulated about 1.5 km of displacement. We used structural, petrographic, isotopic, microthermometric, compositional and organic matter analyses to constrain fluid and host rock properties during fault zone evolution. This approach allowed us to quantify the thermal anomaly in the fault zone and to infer the processes responsible for such a disequilibrium. Specifically, we show that in the fault process zone ahead of the upper fault tip, which is twice as wide as the damage zone, seismic pumping caused suprahydrostatic fluid pressures and that local dilation promoted the nucleation of a highly permeable mesh of conjugate extensional shear fractures hosting calc-silicate mineralization. The thermal difference between hydrothermal minerals in the conjugate fracture mesh and the host rock is 60-90 °C. The mineralizing fluids were deeply-sourced from metamorphic reactions. Propagation of the upper fault tip caused process zone folding and incorporation into the fault damage zones. As the upper fault tip breached through shallower structural levels, it favored mixing between deep and meteoric fluids.

1. INTRODUCTION

Fluid-rock interactions have been widely studied to better understand fluid migration and accumulation and their effects on compositional, petrophysical and rheological rock modifications during deformation (Nesbitt and Muehlenbachs, 1989; Evans and Battles, 1999, Roure et al., 2005; Vilasi et al., 2009; Vandeginste et al., 2012). Textural, geochemical and microthermometric analyses of syntectonic vein cements allow constraint of paleofluid properties, such as their origin, migration pathways, temperature and pressure of crystallization and the local state of stress during deformation (Mullis, 1979, 1987, 1988; Carter and Dworkin, 1990; Fisher et al., 1995; Muchez et al., 1995; Milliken et al., 1998; Montomoli et al., 2001; Montomoli, 2002; Clemenzi et al., 2014; Honlet et al., 2017). In particular, when deformation is thick-skinned, regional-scale fault systems with kilometric offsets are characterized by highly-connected fracture networks in their damage zones, which are preferential sites for fluid migration and mixing from the metamorphic basement up to surficial aquifers (Gratier et al., 2002; Beaudoin et al., 2011; Doglioni et al., 2014; Mamadou et al., 2016; Laurent et al., 2017; Wüstefeld et al., 2017). Cements hosted in fault-related fractures commonly record a multi-stage paleofluid and deformational evolution characterized by dissolution-reprecipitation processes and repeated, episodic fracturing (Phillips, 1972; Ramsay, 1980; Parry and Bruhn, 1987; Fisher et al., 1995; Parry, 1998). The latter can be related to the earthquake cycle that, depending on whether seismic pumping or fault-valve occurred (Sibson et al., 1975, 1988), causes high fluid pressures in fault zones after or before earthquake ruptures, respectively (McCaig, 1988; Boullier and Robert, 1992; Cox, 1995; Robert et al., 1995; Cox, 1999). Therefore, cement patterns in seismically active fault damage zones can provide important exhumed analogues to better understand the properties of fluids involved in seismic ruptures at depth. The permeability of fault zones major components, which can act as either conduits, barriers or mixed conduits-barriers systems, exerts a first-order control on the generation of fluid pressures and fluid flow. Fault zones with kilometric displacement affecting sandstones are typically characterized by low-permeability cores and highly-permeable damage zones (Caine et al., 1996; Faulkner and Rutter, 2001; Faulkner et al., 2010). The latter, however, are heterogeneous rock volumes, which can be subdivided in wall damage zones, tip damage zones and linking damage zones (*sensu* Kim et al., 2004) according to their structural position. Tip damage zones, or process zones (*sensu* Cowie and Shipton, 1998) and linking damage zones, at the tips of propagating faults, have higher permeability due to extensive fracture nucleation with multiple orientations and are preferential sites for fluid flow compared to wall damage zones (Curewitz and Karson, 1997). Accordingly, process zones and linking damage zones can enhance deep fluid advection, producing positive temperature anomalies and chemical and barometric disequilibrium between fluids and host rocks. However, fluid sources and pathways and, consequently, the scales of fault-controlled fluid flow deserve further investigations, as well as the relationships between vein infilling phases and damage zone evolution during fault growth.

In this contribution we present the results of a study of the structural architecture and paleofluid evolution recorded in fault-related veins of the Compione fault zone, a segment of the about 30 km long Northern Lunigiana high-angle basin-boundary extensional fault system cross-cutting the whole nappe pile in the inner portion of the Northern Apennines (Fig.1). The Northern Lunigiana Fault started developing since Early Pliocene times during the uplift and exhumation of the Apenninic tectonic wedge and is still active today (Boncio et al., 2000; Eva et al., 2014; Bonini et al., 2013). The Compione Fault accumulated about 1.5 km of displacement (Bernini and Lasagna, 1988; Bernini, 1991; Bernini and Papani, 2002) and offers suitable exposure conditions for performing a representative structural transect across the fault zone. A multidisciplinary dataset was collected, including independent geothermometers to evaluate thermal anomalies, and geochemical analysis to constrain the fluid sources. Structural analysis was combined with vein cement petrography and optical cold cathodoluminescence, SEM-EDS analysis, carbon and oxygen stable isotope analysis and microthermometry. Moreover, maximum paleotemperatures recorded in the Macigno Sandstones Formation were constrained by vitrinite reflectance of organic matter and thermal modeling.

Our results show that hydrothermal calc-silicate mineralization occurred in the process zone fracture mesh during upward propagation of the Compione Fault, from fluids at temperatures higher than at the burial peak in the host rock and synchronously with methane migration. Crystallization temperatures of hydrothermal minerals in the footwall damage zone record the progressive cooling/exhumation and folding of the process zone fracture network by extensional fault-propagation folding (Withjack et al., 1990; Schlische, 1995; Hardy and McClay, 1999; Ferrill et al., 2004a; Jin and Groshong, 2006), causing shear reactivation of favorably oriented hydrothermal fractures. We propose a model where mineralization preferentially forms in process zones ahead of propagating fault-tips and fluids responsible for fault-related mineralization are supplied by the metamorphic basement and by the different stratigraphic horizons cut by the fault zone through a seismic pumping mechanism.

2. GEOLOGIC SETTING

The Apennines segments of the Alpine-Himalayan orogenic belt were growing in Cenozoic times due to the southwestward subduction and related slab retreat of the Adria micro-plate below the overriding European plate (Principi and Treves, 1984; Malinverno and Ryan, 1986; Royden, 1988; Dewey et al., 1989; Patacca et al., 1990; Doglioni, 1991; Jolivet et al., 1998). Two major paleogeographic domains are telescoped in the Apennines: the ocean-derived Jurassic to Paleogene Ligurian succession and the Adria passive margin domain (Boccaletti et al., 1971; Elter and Pertusati, 1973, Elter et al., 1975). The Subligurian domain was originally located in the ocean-continent transition (Plesi, 1975; Montanari and Rossi, 1982; Vescovi, 1998). Building up of the Northern Apennines thrust wedge included underthrusting up to 15-20 km depth and greenschist facies metamorphism (Apuan Alps in Fig. 1; Di Pisa et al., 1985; Franceschelli et al., 1986; Jolivet et al., 1998; Molli et al., 2000a, 2000b, 2002); while the non-metamorphic successions (Tuscan, Subligurian, Ligurian, Epiligurian successions in Fig. 1) were affected by synorogenic extension episodes (Carmignani and Kligfield, 1990; Carmignani et al., 1994; Decandia et al., 1998; Jolivet et al., 1998; Molli, 2008; Clemenzi et al., 2014) and out-of-sequence thrusting (Storti, 1995; Argnani, 2002; Boccaletti et al., 2011; Bonini et al., 2013; Clemenzi et al., 2014). Extensional faulting and magmatism took place since upper Miocene to Pleistocene times and migrated northeastward behind the advancing thrust fronts (Elter et al., 1975; Serri et al., 1993; Bartole, 1995; Carmignani et al., 1995; Barchi et al., 1998; Martini et al., 2001).

Conditions of deformation in the non-metamorphic, dominantly carbonatic thrust sheets of the Northern Apennines have been determined through different methodologies: vitrinite reflectance

(Reutter et al., 1981; Corrado et al., 2010; Carlini et al., 2013), illite crystallinity (Cerrina Feroni et al., 1983; Carosi et al., 2003; Carlini et al., 2013), stable isotopes (Carter and Dworkin, 1990; Milliken et al., 1998; Mazzarini et al., 2010; Clemenzi et al., 2014), calcite-dolomite geothermometry (Carosi et al., 2003), fluid inclusion microthermometry (Montomoli et al., 2001; Montomoli, 2002; Mazzarini et al., 2010; Clemenzi et al., 2014) and apatite and zircon fission tracks (Abbate et al., 1994; Zattin et al., 2002; Balestrieri et al., 2003; Bernet et al., 2004; Fellin et al., 2007; Corrado et al., 2010; Thomson et al., 2010; Carlini et al., 2013). The estimated maximum burial is about 7 km at temperatures ranging between 200 and 250 °C. Geothermal gradients calculated with different methodologies span a wide range from 18 °C/km to 41 °C/km with a mean value of 31 ± 4 °C/km (Molli et al., 2011).

2.1 The Northern Lunigiana Basin

The Northern Lunigiana Extensional Basin (NLB) is about 25 km long and 10 to 15 km wide. It is the northwesternmost onshore extensional basin in the Northern Apeninnes and is located to the northwest of the Alpi Apuane metamorphic complex, on the Tyrrhenian Sea side of the orogenic wedge (Fig. 1). The Northern Lunigiana Basin is separated from the Southern Lunigiana Basin by the Secchia transversal line (Fig. 1B; Ghelardoni, 1965). The Northern Lunigiana Basin developed in the hanging wall of a regional-scale out-of-sequence thrust (Storti, 1995; Vescovi, 2005; Clemenzi et al., 2014; Molli et al., 2018) that caused duplexing of the Northern Apennines nappe pile, i.e. subligurian rocks overthrusting the Adria-derived Tuscan succession and overlain by Ligurian thrust sheets (Fig. 1D). As a result of such multiple thrusting events, the basin-boundary fault system juxtaposes the Cretaceous Ligurian Ottone Flysch Formation in the hanging wall, against the Late Oligocene-Early Miocene Macigno Sandstones Formation in the footwall (Figs. 1B and 1D; Elter and Schwab, 1959; Giglia, 1974; Elter et al., 1975; Bernini and Lasagna, 1988). The Campanian to early Maastrichtian Ottone Flysch Formation has a maximum thickness of 300-400 m and is composed of marly-calcareous turbiditic and calcarenitic to lithoarenitic strata. The Chattian to Aquitanian Macigno Sandstones Formation is in the studied area about 2300 m thick and is composed of massive sandstone strata in the lower and upper part of the formation, separated by clay- and silt-rich strata (Ghibaudo, 1980). Massive sandstone beds are up to 5 m thick, while the silty and clayey facies beds are a centimetre up to maximum 1.5 m thick. Macigno Sandstones are arkoses and contain abundant quartz, feldspars, biotite, muscovite and chlorite.

The onset of extension in the NLB has been dated using palynology and mammal fauna (Azzaroli, 1950, 1977; Federici, 1978, 1981; Raggi, 1985; Bertoldi, 1988, 1995) in the fluvial-lacustrine deposits that rest on the Ottone Flysch Formation in the depressed central area. These data indicate that two sub-basins developed in response to extensional tectonics: Aulla-Olivola in the SE and Pontremoli in the NW, starting from Early Pliocene and Early Pleistocene times respectively. The deposits follow a regressive trend from lacustrine to alluvial-fan at the top. In the SE they are characterized by two unconformities, the first Late Pliocene in age and the second dated at Middle-Pleistocene times, which occurs also in the Pontremoli depocenter (Boccaletti et al., 1992; Boccaletti and Sani, 1998; Bernini and Papani, 2002). Extension is interpreted to be active during a general uplifting phase of the inner Apenninic belt (Bartolini et al., 1982; Cerrina Feroni et al., 1983; Bernini et al., 1990; Di Naccio et al., 2013).

Both the Northern and the Southern Lunigiana extensional basins are tectonically active, as indicated by extensional earthquakes occurring at depths typically shallower than 15 km, as well as few contractional ones having their hypocenters at about 50 km (Bossolasco et al., 1973; Bossolasco et al., 1974; Augliera et al., 1990; Frepoli and Amato, 1997; Boncio et al., 2000; Eva et al., 2014; Bonini et al., 2013). This is further supported by morphotectonic evidence (Di Naccio et al., 2013). The NLB formed above a northeastward-dipping low-angle detachment fault (Artoni et al., 1992; Camurri et al., 2001; Argnani et al., 2003; Di Naccio et al., 2013) and it attains a half-graben geometry produced by the activity of the NW-SE striking, SW dipping Northern Lunigiana basin-boundary extensional fault system (Bernini, 1988; Bernini and Lasagna, 1988; Bernini, 1991; Bernini and Papani, 2002). The asymmetric topography, with the Apenninic watershed to the NE (Fig. 1D), the northeastward tilt of syn-extensional deposits (Bernini, 1988) and morphotectonic evidence (Di Naccio et al., 2013) support the importance of the Northern Lunigiana extensional fault system in controlling the development of the NLB. In the study area, the NLB is bounded to the NE by the Compione Fault (Figs. 1B, 1D, 2 and Fig. DR1[1]) which can be considered the SE prosecution of the Groppodalosio fault (Fig. 3). Subsurface information provided by a seismic line located in the study area (Figs. 1B, 2) is quite scarce due to the poorly imaged geological complexity of the region (Fig. 2). The proposed geometry shows the Compione Fault cutting through the thrust sheet pile and penetrating into the seismic basement, as previously mapped (Argnani et al.; 2003; Camurri et al., 2001), at around 6 to 7 km depth with an almost planar geometry (Fig. 2), confirming its role in shaping the NLB. At the surface, the Compione Fault is located at the forelimb-crest transition of the anticline associated with the regional-scale out-of-sequence thrust (Figs. 1D; 3A and 3B; Vescovi, 2005; Clemenzi et al., 2014; Molli et al., 2018). Synthetic fault zones occur in the footwall, whereas several synthetic and antithetic fault zones dissect the hanging wall (Bernini, 1991; Bernini and Papani, 2002).

3. METHODS

3.1 Structural Analysis

About 600 structural data were collected at six structural sites, five of which located in the fault damage zones and one in the footwall host-rock, for comparative purposes. Structural data are reported according to the right-hand rule (strike/dip), and stereographic projections (lower hemisphere of Schmidt net) are plotted with the Daisy3 software (Salvini, 2017).

3.2 Petrography and Cathodoluminescence

Fifty veins were sampled in fault damage zones and in the hanging wall host rocks. Moreover, three more sampling sites were identified along strike of the footwall damage zone, to the west of the study transect, at a distance of 0.7, 1.75 and 15 km from it (Figs. 3A and 3C). Each sample was cut in two slabs, one of which was stained with Alizarin Red S and potassium ferricyanide to discriminate the different carbonates such as calcite and dolomite and their iron-rich equivalents (Dickson, 1966). Thin sections and wafers were obtained from the other slab. Petrographic and microstructural analyses were carried out on fifty 30 μm thick thin sections, through standard optical and cold CL microscopy. A Zeiss Axioplan 2 microscope was used for optical petrography. A Technosyn 8200 Mark II cold CL stage, mounted on a LEICA DM2700P optical microscope, was used at 15 kV and 220-250 μA gun current to perform CL analysis. Compositional analyses were carried out on prehnites with a Jeol 6400 SEM equipped with an Oxford EDS. Operating conditions were 15 kV and 1.2 nA, an electron beam with a diameter of about 1 μm and a counting time of 100 s. Errors are ±2–5% for major elements and ±5–10% for minor components. Standards used to calibrate the EDS include pure elements, simple oxides and simple silicate compositions (cobalt, anorthoclase, apatite, augite, microcline and olivine).

3.3 Carbon and Oxygen Stable Isotopes

Stable isotope analyses for oxygen and carbon were performed on host rocks carbonate components and on calcite cements previously identified by petrography and CL. Carbon isotope results are expressed in Vienna Pee Dee Belemnite (V-PDB) while oxygen isotope results are expressed both in V-PDB and in Vienna Standard Mean Ocean Water (V-SMOW) for convention purposes. $\delta^{18}O$ values were converted using the equation (Friedman and O'Neil, 1977):

$$\delta^{18}O\ SMOW = 1.03086 \cdot \delta^{18}O\ VPDB + 30.86 \qquad (1)$$

Stable isotope analyses for oxygen and carbon (cf. paragraph 5.2) were carried out on 98 sub-samples of veins and host rocks. Sub-samples were drilled directly from 33 thin sections using an ESI New Wave Research Micromill with a 6.7X to 40X optical zoom, 3.3 mm to 24.5 mm field-of-view, automated 50 mm travel in X, Y and Z directions stage with sub-micron step resolution and a milling chuck speed ranging from 1200 rpm to 35000 rpm. 100-150 μg of pure carbonate powder for each sub-sample were loaded into a GasBenchII autosampler interspaced with three isotopically different kinds of reference materials (NBS18, NBS19 and MAB99). After flushing the vessels with ultrapure helium (5.5 grade) in order to replace the air, powders were reacted with 100% orthophosphoric acid at 25 °C for 12 h (McCrea, 1950). Resulting gases were analyzed automatically using a Thermo Finnigan Delta V+ mass spectrometer. For each sample, four reference gas peaks were measured and the sample gas was introduced ten times into the mass spectrometer. Each sample was analyzed at least in double so the uncertainty on the samples value may be considered ±0.10‰ and ±0.23‰ for $\delta^{13}C$ and $\delta^{18}O$ respectively. Isotope fractionation curves were calculated according to O'Neil et al. (1969).

3.4 Micro-Raman

Micro-Raman measurements were performed using a Jobin-Yvon Horiba LabRam spectrometer equipped with a He-Ne laser (emission line 632.8 nm) and motorized XY stage. The spectral resolution is about 2 cm^{-1}. The confocal hole was adjusted in order to obtain a spatial resolution (lateral and depth) of 1-2 μm. Spectra were obtained using a 50X objective (0.75 N.A. [numerical aperture]). The calibration was made using the 520.7 cm^{-1} Raman line of silicon. The scanned spectral range spans from 1100 to 3300 cm^{-1}. Acquisition time was 120 s. The power on the sample surface is around 1 mW but the power on the analysed inclusions has to be considered lower due light reflection and scattering.

3.5 Fluid Inclusion Microthermometry

Fluid inclusions were studied in 44 wafers, i.e. doubly polished sections with a thickness of about 100 μm. Fluid inclusion petrography was carried out on a standard petrographic microscope in order to distinguish assemblages, trails and isolated inclusions. Fluid inclusion assemblages (FIAs) are groups of inclusions that occur along growth zones or randomly in the minerals and represent the fluid conditions during precipitation or recrystallization (Goldstein and Reynolds, 1994). FIAs were systematically measured. Fluid inclusion trails (FITs) are related to fracturing events after crystallization of at least part of the host mineral and were not considered during microthermometric analysis. Isolated inclusions were measured and were considered reliable if they showed comparable temperatures to the inclusions organized in FIAs in the same sample. After fluid inclusion petrography, the doubly polished wafers were broken in smaller pieces (chips) and analyzed in a Linkam THMSG600 heating-freezing stage. The instrument was calibrated weekly using SynFlinc synthetic standards. Calibration lines were calculated from melting temperature of CO_2, final melting temperature of clathrate, homogenization temperature of CO_2, NaCl eutectic temperature, final ice melting temperature of pure H_2O and the critical homogenization temperature of pure H_2O. Three temperatures were acquired in aqueous biphase inclusions: 1) homogenization into the liquid phase (Th_{tot}) indicating the minimum temperature of fluid entrapment; 2) first melting temperature (Tfm), related to the fluid composition; 3) ice melting temperature (Tm_{ice}), which is inversely proportional to the amount of solutes in the liquid phase, i.e. the salinity of the fluid. Heating was always performed before freezing runs to avoid artificial stretching of the inclusions during freezing. Monophase gaseous inclusions at room temperature develop a liquid meniscus during cooling in the heating-freezing stage. In these gaseous inclusions, only Th_{tot} was measured and homogenization occurred into the vapour phase. Monophase aqueous inclusions were kept in a freezer for 2 weeks at -20 °C to nucleate bubbles in metastable inclusions. Inclusions that did not nucleate the vapour phase, were cyclically heated and frozen to induce artificial stretching. In this way, it was possible to measure Tm_{ice} in monophase inclusions. Homogenization temperatures are evidently not measured in artificially stretched aqueous inclusions. Accuracy of measurements is ± 2 °C for homogenization temperatures (Th_{tot}) and ± 0.2 °C for first melting (Tfm) and ice melting temperatures (Tm_{ice}).

3.6 Organic Matter Optical Analysis and Thermal Modelling

Ten organic-rich laminae were sampled in the footwall damage zone (Sites 4 and 5) and in the footwall host rock (Site 14) to constrain the thermal maturity of the Macigno Sandstones Formation through vitrinite reflectance analyses. Vitrinite is the product of thermal maturation of terrestrial plant remnants included in sediments and it is one of the most reliable indicator of peak temperatures at maximum burial depth because it is very sensitive to temperature increase and not affected by retrograde processes (Tissot and Welte, 1984; Teichmüller, 1987). Samples for vitrinite reflectance analyses were crushed and then mounted in epoxy resin and polished, according to the method of Bustin et al. (1990). Samples were analysed in reflected, non-polarized, monochromatic light (λ = 546 nm) under oil immersion (ν = 1.518) using a Zeiss Axioplan MPM400 microscope equipped with a J&M Analytik Tidas S 800 spectrometer and calibrated with CRAIC vitrinite reflectance standards. Up to 40 Ro% (randomly oriented vitrinite reflectance in oil immersion) measurements per sample were acquired. Thermal modeling was carried out using the BasinMod2 software, based on the Easy%Ro kinetic model of Burnham and Sweeney (1989). The software requires organic maturity indicators, sedimentary successions lithologies, thicknesses and ages along with paleo-heat flow or paleo-geothermal gradient as basic input data. Sample stratigraphic locations were modelled as a pseudo-well according to Oncken, 1982; Di Paolo et al., 2012; Caricchi et al., 2015; Schito et al., 2018. The main assumptions for the modeling are: (1) decompaction of the burial curves is corrected according to the method of Sclater and Christie

(1980); (2) sea-level changes are neglected, as the thermal evolution is influenced more by sediment thickness than water depth (Butler, 1992); (3) thrusting is considered instantaneous when compared with the duration of sedimentation, as generally suggested in theoretical models (Endignoux and Wolf, 1990); (4) geothermal gradient (25-30°C/km) is calculated from the correlation of vitrinite reflectance data based on the kinetic model of vitrinite maturation of Burnham and Sweeney (1989).

4. STRUCTURAL ARCHITECTURE OF THE COMPIONE FAULT

The area near Compione village was mapped in detail to describe the structural architecture of the Compione Fault, which strikes ~NW-SE and dips to the SW (Fig. 3C). The two different lithologies observed determine different deformation patterns in the footwall and in the hanging wall, respectively (Figs. 4A-C). In the footwall, Macigno Sandstones Formation strata dip 5°-10° towards the NE in the footwall far from the fault zone. Approaching the footwall damage zone, bedding is progressively tilted towards the SW to become horizontal at around 0.7 km distance from the fault core, then SW-dipping of ~40° at around 0.5 km, and up to 55° at the damage zone-fault core transition. Similarly, the Ottone Flysch Formation in the hangingwall is characterized by strata that dip ~60° SW in proximity of the fault core and become subhorizontal outside the hanging wall damage zone (Figs. 3B and 3C). A major E-W striking, S dipping fault zone occurs to the ESE of Compione village (Fig. 4C), abutting the Compione Fault, as well as subsidiary fault segments, to the south (Fig. 3C). The Compione fault zone has a core of up to 50 meters wide, consisting of deformed shear lenses of mostly Macigno Sandstones Formation, bounded by anastomosed shear bands of comminuted, incoherent sand and gouge (Bernini and Lasagna, 1988). In the northwestern corner of the map, the Compione Fault affects a Pleistocene conglomerate consisting of boulders and pebbles of Macigno Sandstones Formation, named Iera Conglomerate (Fig. 3C, Bernini and Papani, 2002)

4.1 Footwall Damage Zone

The most abundant deformation structures in the footwall damage zone are conjugate shear vein pairs inclined at ~60° to bedding in both dipping directions and with bisector lines perpendicular to bedding regardless of bedding dip (Figs. 5A and 5B). Outside the damage zone, 900 meters to the fault core, veins occur only associated to subsidiary extensional faults with metric offset. In the outer boundary area, where strata are subhorizontal, vein orientation is N306°, 60° for the antithetic set and ~N120°-N140°, 60°-80° for the synthetic (Figs. 4A and 5B). Conjugate shear vein arrays are passively rotated with bedding at decreasing distance from the fault core (Figs. 5C and 5D). Such a rotation and the activity of late subsidiary fault zones causes significant dispersion of vein strike, which varies from NNW-SSE to E-W. This is evident when shear vein data collected in subsidiary fault-bounded blocks to the north and south of the major E-W striking fault zone are rotated to restore local bedding attitude to horizontal (Fig. 6). The dip direction in non-rotated data varies from north- to eastward (Fig. 6A). Rotation systematically produces conjugate arrays striking either NW-SE or E-W, respectively (Fig. 6B). In addition to fault-parallel conjugate shear vein arrays, cross-fault veins striking almost perpendicular to the Compione Fault are also abundant (Fig. 4).

Most fault-related veins are reactivated as strike-slip (cross-fault veins) or conjugate extensional faults (fault-parallel veins; Fig. 5E). Strike-slip faulting in the area is related both to lateral propagation of the Compione fault zone and to the far-field stress of the left-lateral Secchia transversal line, 4 km to the E of the study area. These fault-related shear veins and faults (extensional and strike-slip) are well developed especially in coarse strata, have offsets ranging from centimetres to meters, and are characterized by millimetre to centimetres slickenfibers. Strike-slip and extensional faults mutually crosscut and their slip surfaces frequently show evidence for variable directions of movement (Fig. 5F). In sites 4 and 5, conjugate extensional faults have a more complex pattern that includes two synthetic trends, oriented 255°, 70° and 290°, 56° and two antithetic ones, oriented 350°, 10° and 240°, 30°, respectively. It is important to note that, after bedding restoration to the horizontal, the synthetic sets are 127°, 75° and 75°, 77° and the antithetic sets are 308°, 60° and 257°, 74°, respectively, and that ~E-W striking conjugate veins show re-activation as strike-slip to oblique-slip subsidiary faults. Reverse kinematics are apparent, indicating that normal to oblique faulting, with top-to-the-WNW shearing, was ongoing during passive bedding rotation in the damage zone sector comprised between the Compione fault core and major E-W footwall splay fault (Fig. 6B). As a result, S and SW dipping extensional faults in Fig. 6B were re-activated antithetically as soon as they attained a NE dipping attitude due to bedding rotation. Late-stage faults strike from N110° to N130°, dip 60-80° either to the NE or SW (Fig. 4) and have cores made of cataclastic loose sand and clay smears, bounded by thin slip zones including extremely comminuted material. These late-stage faults occur up to 400 meters from the fault core.

4.2 Hanging Wall Damage Zone

Subsidiary fault zones mainly arranged in synthetic anastomosed arrays are abundant in the hanging wall damage zone near the fault core, isolating extensional shear lenses affected by intense pressure solution as indicated by abundant shallow-dipping stylolites (Fig. 4). Moving away from the fault core, both synthetic and antithetic subsidiary faults and fault zones occur, frequently with a ramp-flat geometry. Here very thick beds are cut at high angle and the marly and clayish interlayers are exploited as flat segments, (e.g. site 2 in Fig. 4) producing significant block tilting about horizontal axes. Eventually, at about 300-400 m away from the fault core of the Compione Fault, the deformation pattern is dominated by high-angle antithetic faults and fault zones (e.g. site 1 in Fig. 4). Overall, subsidiary faults and fault zones in the hanging wall strike NW-SE, i.e. parallel to the master fault strike, with a subordinate population striking ~E-W and dipping S (e.g. site 2 in Fig. 4). Abundant veins nearly perpendicular to bedding occur in the hanging wall and crosscut pre-existing bedding-parallel veins. Both populations grew by crack-seal opening (cf. Ramsay, 1980) before the onset of extensional fault-related deformation, during thrusting and stacking of the Ligurian successions. Subvertical veins are passively rotated in the hanging wall blocks of subsidiary fault zones and are commonly re-activated as low-displacement shear surfaces showing slickensides coherent with extensional, almost dip-slip, kinematics.

5. VEIN CEMENT ANALYSIS

5.1 Petrographic Description

Fault-related veins in the footwall damage zone have an aperture varying from 2 to 27 mm and show evidence for antitaxial multiple opening (cf. Durney and Ramsay, 1973; Ramsay and Huber, 1983; Passchier and Trouw, 2005; Bons et al., 2012). Vein cement consists of prehnite, quartz and three different calcite generations, labelled as MC1A, MC1B and MC2, respectively (Fig. 7A). Prehnite crystals are generally euhedral to subhedral and their dimension can reach 1500 μm parallel to the c axis and 750 μm orthogonal to it. Prehnite was the first mineral phase to crystallize in columnar-radiating structures that are overgrown by or inter-grown with euhedral to subhedral quartz (Figs. 7A and 7B). When analysed in cold CL, prehnite luminescence color switches abruptly from "olive green" to "lime green", from the cores towards the rims (Fig. 7B; Huber et al., 2007). Compositional analyses were carried out by SEM-EDS on three prehnite crystals sampled from site 5. Ten areas were analysed both along the long and the short axes of the crystals to investigate compositional variations during crystallization. Sixty spectra were acquired and eight of them did evidence calcite contamination, which is often found as isomorphous replacement of prehnite (Figs. 7C and 7D). Analyses results did not evidence any trend in amounts of Fe^{3+}- Al^{3+} along crystal axes from the cores to the rims of crystals. Al_2O_3 ranges between 24.5 and 25.5 wt%, with a mean value of 25.07 ± 0.19 wt%. The mean abundance of SiO_2 is 45.04 ± 0.20 wt%, with values ranging between 44.6 and 45.5 wt%. CaO is comprised between 27.3 and 29 wt% and has a mean value of 27.76 ± 0.23, in agreement with the prehnite formula $Ca_2Al_2Si_3O_{10}(OH)_2$. FeO was detected in twenty-four spectra and was always below 1 wt%. Quartz sometimes displays bridge structures, growth competition textures and dissolution embayments (Fig. 7C; Hilgers and Urai, 2002; Bons, 2001; Okamoto and Sekine, 2011). MC1 calcite grew both as isomorphous replacement of prehnite crystals and in the remaining open sites, mostly at the centre of fractures. The latter are characterized by poikilotopic rhomboedric crystals up to 1 cm in dimension with abundant Type I and Type II twinning (cf. Burkhard, 1993; Ferrill et al., 2004b) and sweeping extinction (Figs. 7A, 7C, and 7G). Stained MC1 is pink, (Fig. 7E) indicating that calcite is non-ferroan (Dickson, 1966). MC1 calcite crystals can be subdivided in MC1A and MC1B: B is mostly characterized by twinning Type I and a "clearer texture" compared to A, which displays abundant twinning Type II. Moreover, MC1A has dark red color in CL while MC1B is red to orange (Fig. 7B and 7D). Multiple antitaxial opening events (cf. Holland and Urai, 2010; Virgo et al., 2014) caused the cyclic repetition of prehnite + quartz + MC1 calcites bands infilling the veins (Figs. 7E-G). Shearing of veins caused quartz dynamic recrystallization and formation of straight, micrometric wide mirror surfaces, which truncate vein crystals (Figs. 7E, 7F and 7G). MC2 is the last cement and is composed of microsparitic to blocky calcite up to maximum 500 μm crystal size, sometimes displaying Type I twinning (cf. Burkhard, 1993). MC2 calcite has bright orange to yellow colors under CL and is hosted in sub-millimetric fracture networks that exploit cleavage surfaces orthogonal and parallel to the c axis of prehnite (Fig. 7A), twinning planes in MC1 calcite and re-opened shear surfaces. Even MC2 calcite, in places, occurs as prehnite isomorphous replacement (Figs. 7H). Veins nearest to the fault core are more intensely affected by shearing, quartz recrystallization, isomorphous replacement of prehnite by MC1 crystals and by MC2 calcite cementation (Figs. 7G and 7I). In the fault core, in fact, the host rock is disaggregated and cemented by MC2 calcite, which displays an interparticle cement texture (Fig. 7J). Footwall fault-related veins in silt and clay beds have MC1 and MC2 calcite cements (labelled as Macigno host rock calcite cement), but they show a microsparitic texture, whereas prehnite and quartz are absent.

Hanging wall veins, hosted in the Ottone Flysch Formation, are composed of two generations of calcite, labelled as OC1 and OC2, and contain traces of quartz. OC1 calcite veins are considered for comparative purposes only because they formed before the onset of extensional deformation in the studied area. OC2 calcite veins formed by multiple antitaxial fracturing-precipitation events (cf. Holland and Urai, 2010) and crosscut or run parallel to OC1 calcite (Figs. 7K and 7L). OC2 calcites have a blocky texture with a “clear” appearance and dimensions up to 1 mm (Fig. 7K), showing rarely Type I twinning (cf. Burkhard, 1993). Their color under CL is red, slightly brighter than OC1 calcites, but it changes depending on structural position (Fig. 7L). In particular, samples collected less than 50 meters from the fault core have OC2 calcites with the same dull luminescence as the OC1 calcites. Quartz crystals smaller than 100 μm sometimes occur in association with OC2 calcites (Figs. 7M and 7N). A crack-seal bedding parallel vein in the hanging wall damage zone, in proximity of the fault core, shows quartz associated with OC2 calcite, which preserve the prismatic habit of prehnite, similarly to the footwall damage zone cement textures (Fig. 7N). Moreover, close to the fault core, OC2 calcite cement shows a proto-breccia texture in extensional S-C (S—schistosity, C—cisaillement [French for shear]) lithons (Fig. 7O).

5.2 Stable Isotopes

Results of carbon and oxygen stable isotopes analyses are summarized in Table 1. MC1 calcites have the most depleted $\delta^{18}O$ values, from +11.8‰ to +14.0 V-SMOW while MC2 calcites range from +13.4‰ to +17.9‰ V-SMOW. Mean $\delta^{18}O$ is +13.1‰ and +15.8‰ V-SMOW for MC1 and MC2 calcites respectively (Fig. 8A). $\delta^{13}C$ in footwall MC1 and MC2 calcites ranges from -5.8‰ to -0.9‰ and from -7.1‰ to -0.4‰ V-PDB respectively. Plotting $\delta^{18}O$ vs. distance from the Compione fault core for MC1 and MC2 calcites, a slight trend appears (Fig. 8B). In particular, $\delta^{18}O$ values become enriched approaching the fault core. The same plot for $\delta^{13}C$ shows that MC1 and MC2 calcites are characterized by different values depending on structural position (Fig. 8C). Site 5 is located in a different footwall block, compared to other structural sites, and shows depleted $\delta^{13}C$, ranging from -7.1‰ to -3.8‰ V-PDB, compared to other sampling sites whose $\delta^{13}C$ is comprised between -2.8‰ and -0.4‰ V-PDB (Fig. 8C). MC1 and MC2 calcites from a sample collected near the NW tip of the Compione Fault (Site 13) have $\delta^{18}O$ and $\delta^{13}C$ values that are enriched compared to the bulk of the samples that are located along the studied cross-section of the fault zone (Fig. 8A). The footwall host rock carbonate component is composed of microsparitic calcite crystals, present in silt and clay-sized intervals. It shows $\delta^{18}O$ values between +13.9‰ and +16.0‰ V-SMOW and $\delta^{13}C$ from -3.2‰ to -0.7‰ V-PDB.

Hanging wall OC1 and OC2 calcites present enriched and more clustered $\delta^{18}O$ and $\delta^{13}C$ values compared to footwall MC1 and MC2 calcite veins. $\delta^{13}C$ values are comparable for hanging wall host rock and both the hanging wall OC1 and OC2 calcite generations. $\delta^{13}C$ in hanging wall carbonates ranges mostly between +1.2‰ and +2.4‰ V-PDB, excluding outliers. Mean $\delta^{13}C$ is +1.9‰ V-PDB for hanging wall host rock and OC1 calcites, and +1.8‰ V-PDB for OC2 calcites. $\delta^{18}O$ values, however, display large variability between hanging wall host rock, OC1, and OC2 calcites, defining a clear horizontally elongated trend in Fig. 8A. Host rock $\delta^{18}O$ is between +26.9‰ and +27.5‰ V-SMOW; OC1 calcites $\delta^{18}O$ are similar to the host rock, ranging from +23.5‰ to +26.9‰ V-SMOW, while OC2 calcites show depleted $\delta^{18}O$ values, comprised between +13.1‰ and +19.7‰ V-SMOW (Fig. 8A). Mean $\delta^{18}O$ are +25.7‰ and +16.5‰ V-SMOW for OC1 and OC2 calcites, respectively. The OC2 outlier has a $\delta^{13}C$ value of -0.46‰ V-PDB, comparable to footwall fault-related veins and corresponds to the replacive calcite, associated with quartz, shown in Fig. 7N.

5.3 Fluid Inclusions

Microthermometry measurements were done on 11 footwall and on 6 hanging wall veins and their results are summarized in Table 2. Quartz in footwall veins shows abundant and clearly visible trails of decrepitated and leaked inclusions. Two types of inclusions have been recognized: biphase aqueous (Q1) and monophase gaseous (Q2). Both of them have a maximum length ranging from 5 to 15 μm and rounded shapes (Figs. 9A and 9C). Only one Q1 primary FIA and two isolated inclusions were large enough to be measured. Vapour to liquid phase ratios are constant and the vapour bubble is less than 15% of the total inclusion volume. Homogenization, always into the liquid phase, occurs between 127 °C and 215 °C (Fig. 10B) with a mean value of 157 °C. First melting temperatures are in the range of -50 °C to -45 °C, suggesting a NaCl-$CaCl_2$-H_2O system (Roedder, 1984), and are followed by the hydrohalite melting temperature between -32 °C and -28 °C. Ice melting temperatures range from -4.8 °C to -11.4 °C (Fig. 10C) with a mean value of -7.2 °C, which corresponds to salinities of 7.6, 15.4 and 10.7 wt% NaCl eq., respectively (Bodnar, 1993). Q2 monophase gaseous inclusions have dimensions similar to Q1 inclusions and a rounded shape. They were measured in three FIAs. Homogenization was into the vapour phase at temperatures ranging from -89 °C to -83 °C (Fig. 10A). Mean homogenization temperature is -88 °C. No solid was formed in these gaseous inclusions. Q2 inclusions were analysed through micro-Raman spectroscopy to check their composition. Results of Raman analysis are briefly illustrated in Fig. 9B and show a peak at 2914 cm^{-1}, which corresponds to the Raman shift of CH_4. Homogenization temperatures, in agreement with Raman results, indicate that Q2 are monophase CH_4 inclusions.

Fluid inclusions in footwall MC1A calcite are biphase aqueous, with a size from 3 μm to 10-15 μm. They have a negative crystal shape and constant vapour/liquid ratio (Fig. 9D). The vapour phase fills 10 to 15% of the inclusion's volume. Inclusions in MC1A calcite are organized in FIAs and in fluid inclusion (FI) trails that follow twinning planes. FI trails and inclusions near twinning planes were not taken into account during microthermometric measurements. Some inclusions leaked at their homogenization temperatures and some bubbles did not reappear upon cooling. These inclusions were also discarded. A total amount of twenty-two MC1A inclusions were measured, distributed in six FIAs and three isolated inclusions. MC1A inclusions show homogenization temperatures ranging from 178 °C to 198 °C. The mean Th_{tot} is 189 °C and the modal peak is between 190 and 195 °C (Fig. 10B). First melting in MC1A inclusions occurred at temperatures between -17 °C and -21 °C, indicating a H_2O-NaCl composition. The MC1A ice melting temperatures range from -0.8 °C to -6.2 °C, corresponding to salinities between 1.4 and 9.3 wt% NaCl eq. Mean Tm_{ice} is -2.7 °C, which corresponds to 4.5 wt% NaCl eq. (Bodnar, 1993; Fig. 10C).

Fluid inclusions hosted in impurity-poor MC1B calcite crystals are slightly smaller than MC1A inclusions, ranging from 2 to 10 μm. They have rounded to negative crystal shape and constant vapour/liquid ratio where vapour fills around 10% of the inclusion's volume. Nineteen MC1B inclusions were measured, distributed in five FIAs. They show homogenization temperatures between 140 °C and 161 °C with a mean value of 151 °C and a modal peak at 150-155 °C (Fig. 10B). First melting temperatures of MC1B inclusions range between -8 °C and -20 °C in three FIAs while they are -31.5 °C in another FIA. Ice melting temperatures for MC1B inclusions range between -0.8 °C and -17.2 °C, which corresponds to salinities ranging from 1.4 to 20.3 wt% NaCl eq. The mean Tm_{ice} is -5 °C, corresponding to 7.9 wt% NaCl eq. (Bodnar, 1993; Fig. 10C). Only the four MC1B inclusions belonging to the FIA characterized by first melting temperatures of -31.5 °C showed Tm_{ice} lower than -6.2 °C, i.e. ranging from -10.1 °C to -17.7 °C.

Footwall MC2 calcite contains biphase aqueous inclusions with the same petrographic characteristics as MC1 inclusions but they were not found aligned in FI trails. Six MC2 FIAs and two isolated inclusions were measured, representing 20 inclusions. They have rounded shapes and dimensions ranging from 2-3 up to 10 μm. Homogenization temperatures range from 69 °C to 115 °C with a mean value of 88 °C (Fig. 10B). Ice melting temperatures range from -0.7 °C to -20.7 °C, corresponding to salinities from 1.2 to 22.9 wt% NaCl eq. The mean Tm_{ice} is -8.7 °C and the mean salinity 12.5 wt% NaCl eq. (Bodnar, 1993) even if the distribution is formed by two clusters, with Tm_{ice} comprised between -16.7 °C and -20.7 °C, and -0.7 °C and -5.8 °C, respectively. The modal peak is comprised between -1 °C and -2 °C (Fig. 10C). MC2 inclusions belonging to the first cluster froze at temperatures lower than -70 °C and showed melting evidence at temperatures comprised between -34 °C and -27 °C as Q1 inclusions. The first melting temperatures were difficult to evaluate but their similar behaviour with Q1 inclusions (this paragraph) suggests a $NaCl$-$CaCl_2$-H_2O system. Only a first melting temperature of -17.8 °C, indicating a $NaCl$-H_2O system, was measurable in MC2 inclusions belonging to the second cluster.

Hanging wall OC2 calcite is characterized by fluid inclusions that are monophase and biphase aqueous with rounded shapes and smaller than 10 μm (Fig. 9F). The vapour phase in biphase inclusions fills 5 to 10% of their volume. Small monophase OC2 inclusions did not nucleate bubbles after two weeks at -20 °C. Two FIAs and an isolated inclusion for a total of sixteen were measured. Homogenization temperatures range from 60 °C to 75 °C in the first FIA and from 110 °C to 115 °C in the second FIA (Fig. 10D). First melting temperature was never observed. Ice melting temperatures range from -1.3 °C to -6.9 °C, with a mean value of -4.4 °C (Fig. 10E) and they correspond respectively to salinities of 2.2, 10.4 and 7 wt% NaCl eq. (Bodnar, 1993). OC2 inclusions have higher salinities at lower homogenization temperatures.

Homogenization vs. ice melting temperatures of measured inclusions are plotted in Fig. 11. Fluid inclusions from quartz in footwall veins show a rather constant salinity, around 10-15 wt% NaCl eq., at different homogenization temperatures. Calcites MC1A, MC1B and MC2 in footwall veins are characterized by a different temperature-salinity trend, generally displaying less than 5 wt% NaCl eq. at 180-200 °C (subgroup MC1A) and an increasingly wider range of salinities at decreasing temperatures. Subgroup MC1B with homogenization temperatures between 140-160 °C, can have salinities up to 20 wt% NaCl eq. At lower temperatures, between 70 and 110 °C, MC2 inclusions have salinities up to 23 wt% NaCl eq. The data belonging to hanging wall fluid inclusions OC2 show a trend similar to footwall calcites, characterized by higher salinities at lower homogenization temperatures.

6. VITRINITE REFLECTANCE AND THERMAL MODELLING

Results of vitrinite reflectance measurements acquired in footwall Macigno Sandstones Formation are summarized in Table 3. Ten samples were analyzed from sites 14, 4 and 5. Samples from sites 4-5 are located in the footwall damage zone while site 14 is located outside the damage zone. Mean values range between 0.42 and 0.70 Ro% and standard deviations are generally below 0.1 Ro%. More in detail, vitrinite reflectance measured on samples in the footwall damage zone (sites 4 and 5) show very dispersed average values ranging from 0.42 to 0.61 Ro% (Table 3), which were based on the in situ vitrinite. The lowest values were measured on very small and fractured fragments with dark oxidized rims along the irregular micro-fissure in the vitrinite particle, making the reflectance assessment scarcely reliable, while only few sufficiently large and unfractured fragments were found showing generally slightly higher values around 0.65-0.70 Ro%. A further family of vitrinite fragments, excluded from the aforementioned average, was found showing values between 1.0 and 1.30 %. These fragments were interpreted as reworked vitrinite.

On the other hand, samples from site 14, far from the damage zone, indicate average values between 0.66 and 0.70 Ro% (Table 3). In situ vitrinite is here represented by large and unfractured fragments even if averages are based on a small number of measurements (between 8 and 19). Also in these samples reworked vitritine showing higher values (between 1.10 and 1.80 Ro%) was found. Nevertheless, the lowest mean values between 0.42 and 0.61 Ro% are found systematically in the footwall damage zone. These values are always associated with oxidized and pervasively fractured vitrinite fragments and thus were not considered in the calibration of the thermal model. Samples in the footwall sandstones outside the Compione fault damage zone, on the other hand, show consistent Ro% values between 0.66 and 0.70.

Assumptions about the burial/exhumation history and heat flow in the MacignoSandstones Formation have to be made, as they are input data necessary for the thermal modelling: (1) stratigraphic location of the samples is comprised between 600 m and 1100 m from the top of the

Macigno Sandstones Formation, which is 2300 m thick (Ghibaudo, 1980). In detail, samples from site 14 are located between 600-800 m and samples from sites 4-5 between 900-1100 m; (2) the Macigno Sandstones Formation was rapidly buried below the 4000-6000-m-thick allochtonous Ligurian and Subligurian units (Carlini et al., 2013); (3) syncontractional exhumation took place up to Late Messinian times through low angle normal faulting in the inner part of the orogenic wedge (Fellin et al., 2007; Carlini et al., 2013; Molli et al., 2018). Moreover, heat flow in the Northern Apeninnes foredeep has values lower than 30°C/km due to rapid burial and thrusting of foredeep units, whose thermal regime is far from equilibrium (Mongelli et al., 1991; Della Vedova et al., 1995).

Ro% values at maximum burial depth could only be fitted using 3000 m of Ligurian and Subligurian units overburden, lower than the minimum thickness estimates of allochtonous units (according to Carlini et al., 2013) and adopting a geothermal gradient of 25-30°C/Km. Thinning of the overburden thickness moving towards the foreland is logical considering the wedge-shaped overall geometry of fold and thrust belts (Davis et al., 1983). The best fit between calculated maturity profile and measured vitrinite reflectance was attained using a geothermal gradient of 25°C/Km up to the end of Miocene that gradually increased up to a present-day value of 30°C/Km. As a consequence, the Macigno Sandstones Formation stratigraphic sector, hosted in the Compione fault footwall damage zone, at 5 km depth, experienced peak temperatures between 140-150°C (Fig. 12).

7. DISCUSSION

7.1 Process Zone Width

An outstanding feature of the Compione Fault is the abundance in the footwall damage zone of veins that, when bedding is rotated to the horizontal, restore to a pattern of conjugate shear fractures with a vertical bisector, i.e. the typical geometry produced in an extensional tectonic regime (Anderson, 1951; Sibson, 1996). This evidence supports vein formation in an early evolutionary stage of the Compione Fault, when bedding in the process zone was still horizontal, before extensional folding and shear localization. Accordingly, the area affected by such extensional shear veins can be interpreted as the process zone sector preserved in the footwall of the Compione Fault, which formed ahead of the upward-propagating master shear zone (cf. Lockner et al., 1992; Reches and Lockner, 1994; Cowie and Shipton, 1998; Vermilye and Scholz, 1998). In the studied across-fault transect, the width of the footwall process zone is about 900 m. The present-day tectonic juxtaposition of the Ottone Flysch Formation in the hanging wall prevents any possibility to quantify the total width of the process zone in the Macigno Sandstones Formation. However, by assuming that the Upper Triassic Burano Evaporites provided a thick plastic layer suitable to enhance initial extensional folding in the overburden (Schlische, 1995; Withjack and Callaway, 2000), it is possible to hypothesize that the tip of the master shear zone was temporarily arrested at the base of the Burano Evaporites while their top, now at around 6 to 7 km depth, provided the apical point of the extensional fault-propagation fold (Fig. 13). By applying the geometric construction of Jin and Groshong (2006) and assuming a linear velocity field in the trishear zone ahead of the propagating upper fault tip (Hardy and Ford, 1997) it is possible to infer a total process zone width of about 1800 m and an apical angle of ~10° (Fig. 13). Taking into account that the total displacement of the Compione Fault is around 1.5 km (Bernini and Lasagna, 1988), our estimate of the process zone width is out-of-scale compared to displacement (D) to damage zone (DZ) ratios reported in the literature, even though D/DZ is strongly dependent on the criteria used to define damage zone thickness and on lithological properties (Knott et al., 1996; Fossen et al., 2007; Childs et al., 2009; Fossen, 2010; Torabi and Berg, 2011; Solum and Huisman, 2016). In fact, assuming that late-stage extensional fault zones are the structural elements that define the damage zone width, then the D/DZ ratio of the Compione Fault would be comparable to those reported in published datasets.

7.2 Cyclical Vein Development and Earthquake Cycle

Footwall damage zone fault-related veins show multiple subparallel fracturing-sealing events indicating that fracturing, cementation, dissolution and shearing were cyclic (Figs. 14A-C; Ramsay, 1980; Boullier and Robert, 1992; Boullier et al., 1994; Sibson, 1996; Renard et al., 2000; Sibson, 2004). The majority of veins is interested by localized shear-reactivation, forming abundant mirror surfaces and, in cases displaying straight micrometric wide slip surfaces truncating crystals, which are interpreted as evidence for coseismic slip (Smith et al., 2011; Fondriest et al., 2013; Smeraglia et al., 2017). Fracturing-sealing cycles caused strain-softening promoting localization of younger fracturing and shearing events at vein-host rock interfaces or in between different openings (Jessell et al., 1994; Virgo et al., 2014). Prehnite exhibits euhedral crystals, organized in columnar-radiating aggregates while quartz shows euhedral to subhedral crystals, in cases also displaying growth competition (Fig. 14A). Both textures require fractures to remain fluid-filled and open during crystal growth (Fisher et al., 1995; Koehn and Passchier, 2000; Oliver and Bons, 2001; Bons et al., 2012), thus implying fluid pressures higher than the local σ_3 for fault-parallel extensional veins. Conversely, blocky rhombohedric calcite texture (Figs. 14A-C), which occludes completely the remaining fracture space, could be caused by different processes: a) supersaturation in response to a pressure drop; b) texture obliteration due to repeated fracturing; c) fast crystal nucleation caused by a sudden arrest of an ascending fluid (Oliver and Bons, 2001). Moreover, prehnite dissolution can promote permeability enhancement and, consequently, pressure reduction (Figs. 14B and 14C; Boullier et al., 1994). In the literature models such as the fault-valve and seismic pumping have been proposed to relate cyclical fracturing-sealing events to the seismic cycle (Sibson et al., 1975, 1988; McCaig, 1988; Boullier and Robert, 1992; Robert et al., 1995; Cox, 1995, 1999).

Our microstructural data support a model of extensional faulting in the upper crust, triggered by shortening and thrusting in a seismically active metamorphic basement (McCaig, 1988). At shallow crustal levels, as in this specific case, fluid pressure is governed by seismic-pumping (Sibson et al., 1975), while the fault-valve mechanism explains supralithostatic pressures at deeper crustal levels (Sibson et al., 1988). In the hypothesis that precipitation of the described prehnite-quartz-calcite assemblages was triggered by seismic activity during upward fault propagation from the basement, silicates (prehnite and quartz) may have crystallized at suprahydrostatic fluid pressure conditions (P_f) after seismically-induced fracturing, i.e. in the post-seismic stages (Figs. 14D and 14E). Suprahydrostatic P_f in the extensional process zone may have been generated by ascending fluids that breached a low-permeability layer at depth (Sibson et al., 1988; McCaig, 1988), reasonably provided by the thick evaporitic sequences at the top of the metamorphic basement, which is deformed in a regional scale antiformal stack structure (e.g. Molli et al., 2018). The decrease of P_f to hydrostatic values led to supersaturation of calcite, which precipitated in the remaining voids thus completing vein infilling and favouring a new cycle of pore fluid pressure increase (Figs. 14D and 14E). The causal link between seismic activity and precipitation of the mineralogical assemblage in rotated shear veins exposed in the footwall damage zone of the Compione Fault is tentatively proposed as a working hypothesis that deserves further studies specifically designed for acquiring a comprehensive dataset suitable to either support or reject this possibility.

7.3 Process Zone Temperature Anomaly

Paleothermal data obtained from the host Macigno Sandstones Formation and from the shear vein network allow estimating the thermal disequilibrium associated with the upward migrating fluids that infiltrated the process zone in the early stages of faulting and related extensional folding.

An anomalous feature is the maturity difference between sites 4 and 5 with respect to site 14, which cannot be explained by different burial since low maturity samples have a lower stratigraphic position. Actually, lower Ro% values from sites 4 and 5 locate into the footwall damage zone and were obtained from very small and fractured fragments with oxidized rims around fractures. This suggests that anomalously low reflectance values are due to oxidation from mixed meteoric and deep fluid weathering occurring probably during the last pulse of fluid circulation around the fault. The increase in permeability during the last stage of the fault's activity created conditions that favoured oxidation of the surface of the organic matter which is subsequently degraded during weathering (Petsch et al., 2000).

Accordingly, the thermal model was calibrated using data from site 14. Thermal modelling of vitrinite reflectance data provided peak temperatures in the footwall damage zone ranging between 140-150 °C at maximum depths of about 5 km and geothermal gradients between 25-30°C/km (Fig. 12). In addition, published data from apatite fission tracks in the Macigno Sandstones Formation sampled in the study area show complete annealing (Thomson et al., 2010; Carlini et al., 2013), which generally indicates temperatures higher than 110 °C (Ketcham et al., 1999). This supports results from our model.

Microthermometric data from quartz Q1 and calcite MC1A cements show homogenization temperatures of 155 °C and 180 °C, respectively. Accordingly, MC1A calcite in the footwall damage zone fracture network shows homogenization temperatures at least 30 °C higher than the surrounding Macigno Sandstones Formation. If we correct data by pressure, assuming that MC1A crystallized crystallized at about 5 km depth in hydrostatic conditions at the onset of exhumation, real fluid trapping temperatures are predicted to be around 210-230 °C (Fig. 15A). Moreover, prehnite in the studied veins, despite the impossibility to provide direct constraints on paleotemperatures may suggest minimum temperature values of about 230 °C based on occurrences in hydrothermal and in geothermal systems in Tuscany, Italy, and other areas showing calc-silicate mineralization (Browne, 1978; Arnason et al., 1994;). It is worth noting that uncertainty is associated with this inference because crystallization conditions might depend on fluid chemistry. Hydrothermalism is abundant and ongoing on the Tyrrhenian Sea side of the Apennines and is related to high-temperature-low-pressure contact metamorphism due to the intrusion of igneous bodies into the crust associated with the Tyrrhenian extension (Cavarretta et al., 1982; Boccaletti et al., 1997; Gianelli et al., 1997; Dini et al., 2005; Boiron et al., 2007 and many others). If our assumptions are correct, then the difference in temperature between hydrothermal fluids that circulated through the fracture network in the process zone and the surrounding host Macigno Sandstones Formation was between 60 and 90 °C. Such a high thermal disequilibrium is supported both by the geometry of the process zone, which displays a low apical angle (Fig. 13), and by supra-hydrostatic fluid pressures that promote fast advection of hot fluids from the basement in a channelized, highly-fractured and narrow deformation zone (Sibson et al., 1988, 1996, 2000; Renard et al., 2000; Gratier et al., 2002; Beaudoin et al., 2011). This result highlights the importance of combining different methodologies to constrain host rock and fault-related fluid paleotemperatures (Mamadou et al., 2016; Honlet et al., 2017; Laurent et al., 2017; Wustefeld et al., 2017).

7.4 Fluid Sources and Migration Pathways

Assuming that Q1 and Q2 inclusions are cogenetic, this would imply that the source fluid underwent fluid immiscibility before entrapment. Cogenetic aqueous biphase and CH_4 gaseous monophase inclusions have already been documented in authigenic quartz in sandstones of the Northern Apennines (Mullis, 1979, 1987, 1988; Montomoli et al., 2001; Montomoli, 2002; Mazzarini et al., 2010). This fluid immiscibility is generally caused by decreasing fluid pressure during upward fluid migration in the fault damage zone, (Parry and Bruhn, 1987, 1990; Sibson et al., 1975, 1988, 2000). MC1B inclusions show the same composition and salinity as MC1A inclusions except for a FIA in Site 5, with higher salinity and lower first melting temperatures, indicating a $NaCl$-$CaCl_2$-H_2O composition as Q1 inclusions.

Assuming equilibrium precipitation, the calculated $\delta^{18}O_{fluid}$ for MC1 calcites is shown in Fig. 15B (Friedman and O'Neil, 1977), and is between +2‰ and +4‰ V-SMOW for MC1A calcite and between 0‰ and +2‰ V-SMOW for MC1B calcite indicating ^{18}O enriched waters due to different degrees of water-rock interaction (e.g. Muchez et al., 1995). Taking into account the different lithologies cut by the Compione Fault (Figs. 1C and 2), $\delta^{13}C$ values of MC1 calcites may indicate different degrees of mixing between methane fluid originating from the thermal maturation of organic matter inside the Macigno Sandstones Formation, inorganic marine carbon-rich fluids from the underlying Mesozoic carbonates and, also, a contribution of metamorphic fluids coming from the basement (cf. Hoefs, 1997; Milliken et al., 1998; Mazzarini et al., 2010; Boschetti et al., 2017). The latter is supported by the occurrence of prehnite crystallization in stage 1, which is a typical mineral of anchizone metamorphism (Merriman and Frey, 1999). Moreover, fluid trapped in MC1A inclusions shows low-salinity and high temperature, which can be ascribed to devolatilization reactions in the underlying metamorphic basement (Walther and Orville, 1982; Oliver, 1996; Connolly, 2010; Ingebritsen and Manning, 2010), while locally higher salinities in MC1B reflect a decreasing contribution of metamorphic fluids.

Hanging wall calcite OC2 is interpreted to be associated with stage 2 on the basis of structural, microstructural and isotopic observations: a) OC2 cements in microfractures that display, locally, quartz crystals along rims; b) OC2 in Fig. 7N occurs, as in the footwall, as isomorphous replacement of prehnite; c) isotopic analysis results of OC2 calcite in the same sample shows a $\delta^{13}C$ shift towards MC1 calcites values indicating local mixing between hanging wall and footwall fluids at stage 2 (Fig. 8). Isotopic results of OC2 calcite show that $\delta^{13}C$ values, except the outlier in Fig. 7N, are similar to OC1 ones, indicating no external source of carbon in the Ottone Flysch Formation. $\delta^{18}O_{fluid}$ from which OC2 precipitated is characterized by a wide variability (Fig. 15B), ranging from around -6‰ to 0‰ V-SMOW. This range could be interpreted as a fluid mix between Ottone Flysch formational waters and meteoric waters ($\delta^{18}O$ around -8‰ to -6‰ V-SMOW, cf. Longinelli and Selmo, 2003; Giustini et al., 2016) even this is difficult to prove since we do not have data on the composition of the fluid.

MC2 calcite crystallized in micro-fractures in the internal footwall damage zone during stage 3. As in stage 1 and 2, even MC2 locally replaces prehnite crystals. The wide range of homogenization temperatures of MC2 inclusions could indicate they were stretched. We, therefore, assume the lower temperatures ranging from 70 to 90 °C as representative for these inclusions. MC2 inclusions with low-salinity (< 10 wt% NaCl eq.) have a NaCl-H_2O composition while those with high-salinity (up to 22.9 wt% NaCl eq.) have a NaCl-$CaCl_2$-H_2O composition. The high salinity could indicate the dissolution of salts in the subsurface (Goldstein and Reynolds, 1994; Boschetti et al., 2017). Carbon forming MC2 calcites was derived from the same sources discussed for MC1 while $\delta^{18}O_{Fluid}$ values, comprised between -6‰ and -2‰ V-SMOW, could indicate mixing between MC1 source fluid and meteoric waters (Fig. 15B).

Phase diagrams of log (a Ca^{2+} / a^2 H^+) vs. log a SiO_2 (aq) in Figs. 16A and 16B have been plotted for, respectively, temperatures of 200 and 150 °C show the stability fields of the mineral assemblages in stage 1 and stage 2. In this framework, at the beginning of stage 1, the upward migrating fault-related fluid is initially recorded by crystallization of prehnite and quartz, which at 200 °C (Fig.16A) are stable at lower log (a Ca^{2+} / a^2 H^+) and log a SiO_2 (aq) compared to 150 °C (Fig.16B; cf. Bird and Helgeson, 1980, 1981; Cavarretta et al., 1982). Then it evolved, at lower temperatures, causing prehnite crystals dissolution and further precipitation of quartz and calcite (MC1 A and B), both in stages 1 and 2. Replacive calcite indicate a dissolution-reprecipitation process, lowering CO_2 content and increasing H_2O, silica and alumina activity in the fluid. Quartz cementation is coeval with upward methane migration which, in contrast, is not recorded in calcite. It can be inferred that quartz crystallization was inhibited when methane was no longer in the fluid and was oxidized to CO_2, necessary to precipitate calcite. Silicates precipitation from an upward migrating and cooling hot fluid is easily explained by decreasing silica solubility at lower temperatures and pressures, while precipitation of calcite, which solubility increases with decreasing temperature and pressure, is promoted by decreasing fCO_2 (cf. Bird and Helgeson, 1980, 1981; Cavarretta et al., 1982).

MC1 and MC2 calcite cements in Site 5, located in the footwall block between the Compione fault core and the E-W footwall splay, show lighter carbon values compared to other sites (Fig. 8C). This $\delta^{13}C$ variation indicates that the sectors of the process zone were characterized by different quantities of organic matter maturation-derived carbon during upward migration. Stable isotope values of MC1 and MC2 in the sample from Groppodalosio (Fault NW tip area, Site 13) are slightly enriched in ^{18}O (triangles in Fig. 8A) compared to Compione, while minimum temperatures of entrapment were the same. Therefore, the $\delta^{18}O_{Fluid}$ composition in the NW were slightly heavier compared to the Compione area.

7.5 Evolutionary Model

The structural fabric preserved in the footwall of the Compione Fault indicates that fault activity in the Macigno Sandstones Formation started with the formation of a km-scale network of shear fractures in conjugate arrays with vertical σ_1 bisector, as expected in extensional Andersonian faulting (Anderson, 1951; Sibson, 1996). The strike of the fractures was mainly parallel to the main trend of the Compione Fault, but also E-W, i.e. parallel to the major footwall fault splay occurring in the study area. This suggests that linkage within and among the major footwall segments constituting the Northern Lunigiana fault system (Fig. 3) occurred in the very early stages of extensional deformation. Such an early fracture network formed the process zone (Lockner et al., 1992; Reches and Lockner, 1994; Cowie and Shipton, 1998; Vermilye and Scholz, 1998) of the Compione Fault in the Macigno Sandstones Formation, ahead of the upward-propagating master fault surface. The process zone was a preferential site for effective fluid circulation and advection of a hydrothermal plume at minimum temperatures of 210-230 °C, i.e. the trapping temperature of MC1A inclusions assuming hydrostatic conditions at 5 km depth, and possibly exceeding ~230 °C, as suggested by fracture cementation with prehnite (Fig. 17A). Results from microthermometry and stable isotope geochemistry indicate an open system circulation with upward directed and channelized high-temperature and low-salinity fluids coming from the metamorphic basement (Mazzarini et al., 2010; Boschetti et al., 2017) which mixed with carbon derived from the maturation of organic matter in the Macigno host rock. Petrographic evidence supports cross-formational fluid flow up to the base of the Ottone Flysch Formation in this early stage.

With increasing extension, the vein network in the process zone was progressively tilted by extensional fault-propagation folding (Withjack et al., 1990; Schlische, 1995; Hardy and McClay, 1999; Ferrill et al., 2004a; Jin and Groshong, 2006) and bedding attained a synthetic dip attitude. During folding, the fault-parallel extensional conjugate vein arrays was preferentially reactivated by antithetic shearing, accompanied by precipitation of quartz and MC1B calcite (Fig. 17B). Mineralization occurred at minimum temperatures between 140 and 160 °C and increasing fluid salinities indicating mixing with a fluid characterized by lower temperature and higher salinity. At this stage there was still stratigraphic continuity across the Compione fault zone, which near surface expression was likely a flexure in the crestal region of the regional-scale anticline deforming the previously stacked thrust sheets of Tuscan and Ligurian rocks. The presence of the clay-rich Subligurian succession at the top of the Macigno Sandstones Formation and the change from siliciclastic to carbonate composition helps explain why conjugate fracture arrays comparable to the underlying ones did not develop in the Ottone Flysch Formation. In the latter, deformation was accommodated through a network of fault segments that partially exploited the pre-existing structural inheritance, accompanied by precipitation of OC2 calcite and rare quartz, at a temperature lower than 110 °C (Fig. 17B).

When bedding dip in the extensional monocline reached values exceeding ~50°, fault propagation and breakthrough was accompanied by formation of a footwall damage zone with a width of about half that of the corresponding process zone. Many rotated shear veins and subsidiary faults were re-activated and together with newly-formed ones, produced a network of high-angle faults with cataclastic cores of disaggregated and gouge layers. MC2 calcite precipitated in fractures of the damage zone, from fluids at temperature between 70° and 90° C, resulting from mixing between deeply-sourced fluids and meteoric waters which likely interacted, at different degrees, with the Burano Evaporites in the subsurface (Fig. 17C). This would explain the high salinity of a low temperature fluid with a stable isotopic composition typical of meteoric fluids. The damage zone in the hanging wall had a comparable width as the footwall but was affected by less intense fracturing, partly replaced by dissolution and discrete subsidiary faulting.

8. CONCLUSION

The Compione Fault is part of the Northern Lunigiana regional-scale extensional fault system, exposed for around 30 km along strike, which accumulated about 1.5 km offset since Early Pliocene times. It is located in the inner portion of the Northern Apennines, at the forelimb-crest transition of a major out-of-sequence thrust-related anticline, that deformed the previously stacked thrust sheet pile. The Compione Fault can be traced in seismic reflection profile down to the seismic basement top at about 6 to 7 km depth and dissects the previously produced contractional architecture. This fault zone offers the possibility to study the interaction between deformation, fluid flow and fracture cementation that progressed from a depth of ~5 km up to near surface conditions. The following major points can be drawn from this multidisciplinary study of the Compione Fault cross-sectional architecture, resulting from the combination of structural, petrographical, geochemical, microthermometric, and paleothermal analyses.

- The footwall damage zone, affecting thick sandstone strata, is characterized by a network of shear veins with bisectors perpendicular to bedding, which was passively rotated by extensional fault-propagation folding during upward fault growth. Such a fracture mesh testifies for the presence of a wide process zone ahead of the fault tip in the early evolutionary stages. A comparable deformation pattern does not occur in the hanging wall damage zone because of either the carbonate composition of the Ottone Flysch Formation that favored an important role of dissolution, or the presence of clay-rich sediments tectonically juxtaposed at its base, which provided a strong mechanical discontinuity, or both.

- Mineralization of the process zone fracture network by a prehnite-quartz-calcite assemblage from a fluid at a minimum temperature of 210 °C, possibly exceeding 230 °C indicates that: (i) the process zone provided a well-connected fracture mesh that significantly improved porosity and favored effective circulation and upward fluid migration; (ii) such a deep fluid volume constituted a hydrothermal plume in strong thermal disequilibrium with the host rock outside the fault zone, which experienced maximum temperatures of less than 140-150 °C.
- Shear vein cementation in the process zone was cyclic and episodic, indicating fluid pressure variations that might relate to the earthquake cycle. According to this hypothesis, seismic pumping may have promoted fast channelized fluid migration from the metamorphic basement, along the fault zone and up to the process zone.
- Synthetic rotation about a horizontal axis of the process zone caused antithetic re-activation of pre-existing shear veins as subsidiary faults and formation of new, non-mineralized high-angle extensional faults. This event of deformation localization represents the formation of the fault damage zones *sensu-stricto*.
- The structural and paleofluid framework exposed in the thick sandstone beds at the footwall of the Compione Fault highlights the importance of the process zone for both fault scaling properties and hydrology. Process zone width is twice that of the damage zone *sensu-stricto*, produced by deformation localization during fault slip. This means that the total volume of footwall fractured rocks, typically included into the damage zone as a whole, is much thicker than what can be expected from statistical scaling laws and has a structural fabric mainly imprinted at the process zone stage. Furthermore, it developed diachronously during fault evolution, with maximum permeability and fluid advection ahead of the upward

propagating fault tip, followed by fracture cementation, deformation localization, and porosity and permeability reduction in more mature stages.

- Development of a process zone at the onset of extensional faulting can significantly contribute creating economically valuable fractured reservoirs ahead of fault tips. Extensional fault-propagation folding favors migration and accumulation of fluids from deeper stratigraphic horizons and the metamorphic basement into the extensional process zone, where high fluid pressures may likely occur. Eventually, fault breakthrough causes reservoir compartmentalization and sealing, preserving favorable conditions for fluid storage in the footwall damage zone and the corresponding process zone sector.
- Depending on the first-order mechanical stratigraphy, development of crustal-scale extensional fault systems can create a strong vertical variability of fractured rock volumes resulting from the interplay among several factors, including: (i) the dominant deformation mechanisms, (ii) fault-propagation versus slip rates, (iii) possible development and width of a vertically-compartmentalized process zone ahead of the upward-migrating fault tip, (iv) competition between faulting and folding, etc. Such a large variability and vertical compartmentalization of the cross-sectional damage zone width strongly impacts fluid storage potential and partitioning in rift-related fault-bounded blocks, as well as the seismic behavior of fault zones.

ACKNOWLEDGMENTS

Discussions with Mahtab Mozafari and Alessandra Montanini on vein cement analysis are gratefully acknowledged. We are indebted to Andrea Comelli for thin section preparation, Enrico Selmo for providing isotopic data, Luca Barchi for support with scanning electron microscopy and Zita Kelemen and Steven Bouillon for help with micromilling equipment. Anna Laura Cazzola, Alessandro Fattorini and Claudio Cattaneo of ENI S.p.A. are thanked for providing reflection seismic data and authorizing their publication and Midland Valley for providing the software Move in the frame of the Academic Software Initiative. Alessio Lucca and Fabrizio Storti ideated the study, collected most of the data and wrote the manuscript, Giancarlo Molli and Fabrizio Balsamo participated to the fieldwork, to data discussion and tectonic interpretations, Philippe Muchez participated to the analysis and interpretation of vein cement petrographic, microthermometric and geochemical data, Andrea Schito and Sveva Corrado provided vitrinite reflectance data and their thermal modelling, and discussed their meaning in the framework of this research, Andrea Artoni depth converted and interpreted reflection seismic data, and Emma Salvioli Mariani helped with Raman spectroscopy and fluid inclusion analysis.

REFERENCES

Abbate, E., Balestrieri, M.L., Bigazzi, G., Norelli, P., and Quercioli, C., 1994, Fission-track dating and recent rapid denudation in Northern Apennines, Italy: Mem. Soc. Geol. It., v. 48, p. 579–585.

Anderson, E.M., 1951, The Dynamics of Faulting and Dyke Formation with Application to Britain (2nd edn): Edinburgh, Scotland, Oliver and Boyd, p. 206.

Argnani, A., 2002, The Northern Apennines and the kinematics of Europe-Africa convergence: Bollettino della Società Geologica Italiana, v. 1, p. 47–60.

Argnani, A., Barbacini, G., Bernini, M., Camurri, F., Ghielmi, M., Papani G., Rizzini F., Rogledi S., and Torelli, L., 2003, Gravity tectonics driven by Quaternary uplift in the Northern Apennines: insights from the La Spezia-Reggio Emilia geo-transect: Quaternary International, v. 101-102, p. 13-26.

Arnason, J.G., Bird, D.K., and Liou, J.G., 1993, Variables Controlling Epidote Composition in Hydrothermal and Low-Pressure Regional Metamorphic Rocks: Abhandlungen der Geologischen Bundesanstalt, v. 49, pp. 17-25.

Artoni, A., Bernini, M., Papani, G., Vescovi, P., and Zanzucchi, G., 1992, Sezione geologica schematica Bonassola (SP)-Felino (PR): Studi Geologici Camerti, Volume Speciale 1992/2, CROP 01-1A, p. 61-63.

Augliera, P., Pastore, S., and Tomaselli, A., 1990, Sismicità della Lunigiana-Garfagnana: Primi risultati da una rete mobile: Proc. 9, Gruppo Naz. Geofis. Della Terra Solida, v. 1, p. 221-232.

Azzaroli, A., 1950, Osservazioni sulla formazione villafranchiana di Olivola in Val di Magra: Atti della Società Toscana di Scienze Naturali Memorie, v. 57, p. 104-111.

Azzaroli, A., 1977, The Villafranchian stage in Italy and the Plio-Pleistocene boundary: Giornale di Geologia, v. 41, p. 61-79.

Balestrieri, M.L., Bernet, M., Brandon, M.T., Picotti, V., Reiners, P., and Zattin, M., 2003, Pliocene and Pleistocene exhumation and uplift of two key areas of the Northern Apennines: Quaternary International, v. 101– 102, p. 67–73.

Barchi, M.R., Minelli, G., and Pialli, G., 1998, The CROP 03 Profile: A synthesis of results on deep structures of the Northern Apennines: Memorie della Società Geologica Italiana, v. 52, p. 383–400.

Bartole, R., 1995, The North Tyrrhenian–Northern Apennines post-collisional system: constraints for a geodynamic model: Terra Nova, v. 7, p. 7-30.

Bartolini, C., Bernini, M., Carloni, G.C., Costantini, A., Federici, P.R., Gasperi, G., Lazzarotto, A., Marchetti, G., Mazzanti, R., Papani, G., Pranzini, G., Rau, A., Sandrelli, F., Vercesi, P.L., Castaldini, D., and Francavilla, F., 1982, Carta Neotettonica dell'Appennino Settentrionale. Note Illustrative: Bolletino della Società Geologica Italiana, v. 101, p. 355-371.

Beaudoin, N., Bellahsen, N., Lacombe, O., and Emmanuel, L., 2011, Fracture-controlled paleohydrogeology in a basement-cored, fault-related fold: Sheep Mountain Anticline, Wyoming, United States: Geochemistry, Geophysics, Geosystems, v. 12, n. 6, Q06011.

Bernet, M., Brandon, M.T., Garver, J.I., and Molitor, B.R., 2004, Fundamentals of detrital zircon fission-track analysis for provenance and exhumation studies with examples from the European Alps, in Bernet M., and Spiegel C., eds., Detrital Thermochronology; Provenance Analysis, Exhumation, and Landscape Evolution of Mountain Belts: Geological Society of America Special Paper 378, p. 25–36.

Bernini, M., 1988, Il bacino dell'Alta Val Magra: primi dati mesostrutturali sulla tettonica distensiva: Boll. Soc. Geol. It., v. 107, p. 355-371.

Bernini, M., and Lasagna, S., 1988, Rilevamento geologico e analisi strutturale del bacino dell'Alta Val Magra tra M. Orsaro e Pontremoli (Appennino Settentrionale): Atti della Società Toscana di Scienze Naturali Memorie, Serie A, 95, p. 139-183.

Bernini, M., Boccaletti, M., Moratti, G., Papani, G., Sani, F., and Torelli, L., 1990, Episodi compressivi neogenico-quaternari nell'area estensionale tirrenica nord-orientale. Dati in mare e a terra: Mem. Soc. Geol. It., v. 45, p. 577-589.

Bernini, M., 1991, Le strutture estensionali della Lunigiana (Appennino Settentrionale): proposta di un modello deformativo: Atti Ticinese di Scienze della Terra, v. 34, p. 29-38.

Bernini, M., and Papani, G., 2002, La distensione della fossa tettonica della Lunigiana nord-occidentale (con Carta Geologica alla scala 1:50.000): Boll. Soc. Geol. It., v. 121, p. 313-341.

Bertoldi, R., 1988, Una sequenza palinologica di età rusciniana nei sedimenti palustri basali del bacino di Aulla-Olivola (Val di Magra): Rivista Italiana di Paleontologia e Stratigrafia, v. 94, p. 105-138.

Bertoldi, R., 1995, Palinostratigrafia dei bacini intramontani dell'Appennino nord-occidentali: Il Quaternario, v. 8, p. 61-70.

Bird, D.K., and Helgeson, H.C., 1980, Chemical interaction of aqueous solutions with epidote-feldspar mineral assemblages in geologic systems. I. Thermodynamic analysis of phase relations in the system CaO-FeO-Fe_2O_3-Al_2O_3-SiO_2-H_2O-CO_2: Am. Jour. Sci., v. 280, p. 907-941.

Bird, D.K., and Helgeson, H.C., 1981, Chemical interaction of aqueous solutions with epidote-feldspar mineral assemblages in geologic systems. II. Equilibrium constraints in metamorphic/geothermal processes: Am. Jour. Sci., v. 281, p. 576-614.

Boccaletti, M., Elter, P., and Guazzone, G., 1971, Plate Tectonic Models for the Development of the Western Alps and Northern Apennines: Nature, v. 234, p. 108-111.

Boccaletti, M., Cerrina Ferroni, A., Martinelli, P., Moratti, G., Plesi, G., and Sani, F., 1992, Late Miocene-Quaternary compressive events in the Tyrrhenian side of the Northern Apennines: Annales Tectonicae, v.6, p. 214-230.

Boccaletti, M., Gianelli, G., and Sani F., 1997, Tectonic regime, granite emplacement and crustal structure in the inner zone of the Northern Apennines (Tuscany, Italy): A new hypothesis: Tectonophysics, v. 270, p. 127-143.

Boccaletti, M., and Sani, F., 1998, Cover Thrust reactivations related to internal basement involvement during Neogene□Quaternary evolution of the Northern Apennines: Tectonics, v. 17, p. 112-130.

Boccaletti, M., Corti, G., and Martelli, L., 2011, Recent and active tectonics of the external zone of the Northern Apennines (Italy): Int. J. Earth Sci., v. 100, p. 1331-1348.

Bodnar, R.J., 1993, Revised equation and table to determine the freezing point depression of H2O-NaCl solutions: Geochim. Cosmochim. Acta, v. 57., pp. 683-684.

Boiron, M.C., Cathelineau, M., Ruggieri, G., Jeanningros, A., Gianelli, G., and Banks, A., 2007, Active contact metamorphism and CO2-CH4 fluid production in the Larderello geothermal field (Italy) at depths between 2.3 and 4 km: Chemical Geology, v. 237, p. 303–327.

Boncio, P., Brozzetti, F., and Lavecchia, G., 2000, Architecture and seismotectonics of a regional low-angle normal fault zone in central Italy: Tectonics, v. 19, p. 1038-1055.

Bonini, M., Moratti, G., Sani, F., and Balestrieri, M.L., 2013, Compression-to-extension record in the late Pliocene–Pleistocene Upper Valdarno Basin (Northern Apennines, Italy): Structural and thermochronological constraints: Italian Journal of Geosciences, v. 132, p. 54–80.

Bons, P.D., 2001, Development of crystal morphology during unitaxial growth in a progressively widening vein: I. The numerical model: Journal of Structural Geology, v. 23, p. 865-872.

Bons, P.D., Elburg, M.A., and Gomez-Rivas, E., 2012, A review of the formation of tectonic veins and their microstructures: Journal of Structural Geology, v. 43, p. 33-62.

Boschetti, T., Toscani, L., Barbieri, M., Mucchino, C., and Marino, T., 2017, Low enthalpy Na-chloride waters from the Lunigiana and Garfagnana grabens, Northern Apennines, Italy: Tracing fluid connections and basement interactions via chemical and isotopic compositions: Journal of Volcanology and Geothermal Research, v. 348, p. 12–25.

Bossolasco, M., Eva, C., and Pasquale, C., 1973, Il terremoto del 25 Ottobre in Lunigiana: Rivista Italiana di Geofisica, v. 22, p. 314-322.

Bossolasco, M., Eva, C., and Pasquale, C., 1974, On seismotectonics of the Alps and Northern Apennines: Rivista Italiana di Geofisica, v. 23(1/2), p. 57-63.

Boullier, A.-M., and Robert, F., 1992, Paleoseismic events recorded in Archean gold-quartz vein networks, Val d'Or, Abitibi, Quebec, Canada: Journal of Structural Geology, v. 14, p. 161-180.

Boullier, A.-M., Charoy, B., and Pollard, P.J., 1994. Fluctuation in porosity and fluid pressure during hydrothermal events: textural evidence in the Emuford District, Australia: Journal of Structural Geology, v. 16 (10), p. 1417-1429.

Browne, P.R.L., 1978, Hydrothermal alteration in active geothermal fields: Ann. Rev. Earth Planet. Sci., v. 6, p. 229-250.

Burkhard, M., 1993, Calcite twins, their geometry, appearance and significance as stress-strain markers and indicators of tectonic regime: a review: Journal of Structural Geology, v. 15, p. 351-368.

Burnham, A.K., and Sweeney, J.J., 1989, A chemical kinetic model of vitrinite maturation and reflectance: Geochimica et Cosmochimica Acta, v. 53, p. 2649–2657, doi: 10 .1016 /0016 -7037 (89)90136 -1.

Bustin, R.M., Barnes, M.A., and Barnes, W.C., 1990, Determining levels of organic diagenesis in sediments and fossil fuels, in McIleareath, I.A., and Morrow, D.W., eds., Diagenesis: Geoscience Canada Reprint Series 4, p. 205–226.

Butler, R.W.H., 1992, Hydrocarbon maturation, migration and tectonic loading in the western Alps, in England, W.A., and Fleet, A.J., eds., Petroleum Migration: Geological Society of London Special Publication 59, p. 227–244.

Caine, J.S., Evans, J.P., and Forster, J.B., 1996, Fault zone architecture and permeability structure: Geology, v. 24, p. 1025-1028.

Camurri, F., Argnani, A., Bernini, M., Papani, G., Rogledi, S., and Torelli, L., 2001, The basement of the NW Apennines: interpretation of reflection seismics and geodynamic implications: Final Proceedings, Geoitalia 2001, 3° Forum Italiano di Scienze della Terra (Fist), Chieti, Italy, p. 50-51.

Caricchi, C., Aldega, L., and Corrado, S., 2015, Reconstruction of maximum burial along the Northern Apennines thrust wedge (Italy) by indicators of thermal exposure and modeling: GSA Bulletin, 127(3-4), 428-442.

Carlini, M., Artoni, A., Aldega, L., Balestrieri, M.L., Corrado, S., Vescovi, P., Bernini, M., and Torelli, L., 2013, Exhumation and reshaping of far-travelled/allochthonous tectonic units in mountain belts. New insights for the relationships between shortening and coeval extension in the western Northern Apennines (Italy): Tectonophysics, v. 608, p. 267–287.

Carmignani, L., and Kligfield, R., 1990, Crustal extension in the Northern Apennines: The transition from compression to extension in the Alpi Apuane core complex: Tectonics, v. 9, p. 1275–1303.

Carmignani, L., Decandia, F.A., Fantozzi, P.L., Lazzarotto, A., Liotta, D., and Meccheri, M., 1994. Tertiary extensional tectonics in Tuscany (Northern Apennines, Italy): Tectonophysics, v. 238, p. 295–315.

Carmignani, L., Decandia, F.A., Disperati, L., Fantozzi, P.L., Lazzarotto, A., Liotta, D., and Oggiano, G., 1995. Relationships between the Tertiary structural evolution of the Sardinia-Corsica-Provençal Domain and the Northern Apennines: Terra Nova, v. 7, no. 2, p. 128–137.

Carosi, R., Leoni, L., Montomoli, C., and Sartori, F., 2003, Very low-grade metamorphism in the Tuscan Nappe, Northern Apennines, Italy. Relationships between deformation and metamorphic indicators in the La Spezia mega-fold: Swiss Bulletin of Mineralogy and Petrology, v. 83, p. 15-32.

Carter, K.E., and Dworkin, S.I., 1990, Channelized fluid flow through shear zones during fluid-enhanced dynamic recrystallization, Northern Apennines, Italy: Geology, v. 18, p. 720–723.

Cavarretta, G., Gianelli, G., and Puxeddu, M., 1982, Formation of authigenic minerals and their use as indicators of the physicochemical parameters of the fluid in the Larderello-Travale geothermal field: Economic Geology, v. 77, p. 1071-1084.

Cerrina Feroni, A., Moratti, G., and Plesi, G., 1983, Evidenze di episodi compressivi messiniano-pliocenici alternati alla tettonica di distensione nella Toscana sud-occidentale, emerse dall'analisi mesostrutturale. In: Atti della riunione su "Meccanismi deformativi nelle catene perimediterranee: stato di avanzamento delle ricerche e problematiche emerse", Firenze, Italy, 5 dicembre 1983, Centro Stampa Palagi Firenze, 35-42.

Childs, C., Manzocchi, T., Walsh, J.J., Bonson, C.G., Nicol, A., and Schopfer, M.P.J., 2009, A geometric model of fault zone and fault rock thickness variations: Journal of Structural Geology, v. 31 (2), p. 117-127.

Clemenzi, L., Molli, G., Storti, F., Muchez, P., Swennen, R., and Torelli, L., 2014, Extensional deformation structures within a convergent orogen: The Val di Lima low-angle normal fault system (Northern Apennines, Italy): Journal of Structural Geology, v. 66, p. 205-222.

Connolly, J.A.D., 2010, The mechanics of metamorphic fluid expulsion: Elements, v. 6, p. 165-172, doi:10.2113/gselements.6.3.165.

Corrado, S., Aldega, L., and Zattin, M., 2010, Sedimentary vs. tectonic burial and exhumation along the Apennines (Italy): Journal of the Virtual Explorer, Electronic Edition, ISSN 1441-8142, v. 36. Paper 15, In: Beltrando M., Peccerillo A., Mattei M., Conticelli S. and Doglioni C., The Geology of Italy.

Cowie, P.A., Shipton, Z.K., 1998, Fault tip displacement gradients and process zone dimension: Journal of Structural Geology, v. 20, p. 983-997.

Cox, S. F., 1995, Faulting processes at high fluid pressures: An example of fault valve behavior from the Wattle Gully Fault, Victoria, Australia: J. Geophys. Res., v. 100, p. 12841-1285.

Cox, S.F., 1999, Deformational controls in the dynamics of fluid flow in mesothermal gold systems, *in* McCaffrey, K., Lonergan, L., and Wilkinson, J., eds., Fractures, Fluid Flow and 1160 Mineralization: Geological Society of London Special Publication, v. 155, p. 123-140.

Curewitz, D., and Karson, J.A., 1997, Structural settings of hydrothermal outflow: Fracture permeability maintained by fault propagation and interaction: Journal of Volcanology and Geothermal research, v. 79, p. 149-168.

Davis, D.M., Suppe, J. and Dahlen, F.A., 1983, Mechanics of fold-and thrust belts and accretionaryw edges: J. Geophys. Res., v. 88, p. 1153-1172.

Decandia, F.A., Lazzarotto, A., and Liotta, D., 1998, The CROP 03 traverse: insights on post-collisional evolution of Northern Apennines: Mem. Soc. Geol. It., v. 52, p. 427–440.

Della Vedova, B., Lucazeau, F., Pasquale, V., Pellis, G., and Verdoya, M., 1995, Heat flow in the tectonic provinces crossed by the southern segment of the European Geotraverse: Tectonophysics, v. 244, p. 57-74.

Dewey, J.F., Helman, M.L., Knott, S.D., Turco, E., and Hutton, D.H.W., 1989, Kinematics of the western Mediterranean, In: Coward M.P., Dietrich D., and Park R.G., eds., Alpine Tectonics: Geological Society of London Special Publication, v. 45, p. 265–283.

Di Naccio, D., Boncio, P., Brozzetti, F., Pazzaglia, F.J., and Lavecchia, G., 2013, Morphotectonic analysis of the Lunigiana and Garfagnana grabens (northern Apennines, Italy): Implications for active normal faulting: Geomorphology, v. 201, p. 293-311.

Di Paolo, L., Aldega, L., Corrado, S., and Mastalerz, M., 2012, Maximum burial and unroofing of Mt. Judica recess area in Sicily: implication for the Apenninic Maghrebian wedge dynamics: Tectonophysics 530-531, 193-207.

Di Pisa, A., Franceschelli, M., Leoni, L., and Meccheri, M., 1985. Regional variation of the metamorphic temperatures across the Tuscanid 1 unit and its implications on the alpine metamorphism (Apuane Alps, N-Tuscany): Neues Jahrbuch für Mineralogie, Abhandlungen, v. 151, p. 197–211.

Dickson, J.A.D., 1966, Carbonate identification and genesis as revealed by staining: Journal of Sedimentary Petrology, v. 32, p. 491-505.

Dini, A., Gianelli, G., Puxeddu, M., and Ruggieri, G., 2005, Origin and evolution of Pliocene-Pleistocene granites from the Larderello geothermal field (Tuscan Magmatic Province, Italy): Lithos, v. 81, p. 1–31.

Doglioni, C., 1991, A proposal for the kinematic modelling of W-dipping subductions - Possible applications to the Tyrrhenian-Apennines system: Terra Nova, v. 3, n. 4, p. 423–434.

Doglioni, C., Barba, S., Carminati, E., and Riguzzi, F., 2014, Fault on–off versus coseismic fluids Reaction: Geosci. Front. V. 5, p. 767–780. http://dx.doi.org/10.1016/j.gsf.2013.08.004.

Durney, D.W., and Ramsay, J.G., 1973, Incremental strains measured by syntectonic crystal growths, In: De Jong K.A., Scholten, K. (Eds.), Gravity and Tectonics, Wiley, New York, USA, p. 67-96.

Elter, P., and Schwab, K., 1959, Note illustrative della Carta Geologica alla scala 1:50.000 della regione Carro-Zeri-Pontremoli: Boll. Soc. Geol. It., v. 78, p. 157-187.

Elter, P., and Pertusati, P., 1973, Considerazioni sul limite Alpi-Appennino e sulle relazioni con l'arco delle Alpi occidentali: Mem. Soc. Geol. It., v. 12, p. 359-375.

Elter, P., Giglia, G., Tongiorgi, M., and Trevisan, L., 1975, Tensional and compressional areas in recent (Tortonian to present) evolution of Northern Apennines: Boll. Geofis. Teor. Appl, v. 17, p. 13-18.

Endignoux, L., and Wolf, S., 1990, Thermal and kinematic evolution of thrust basins: a 2D numerical model, In: Petroleum and Tectonics in Mobile Belts, J. Letouezy (Ed.) and Editions Technip, Paris, France, 181-192.

Eva, E., Solarion, S., and Boncio, P., 2014, HypoDD relocated seismicity in northern Apennines, (Italy) preceding the 2013: seismotectonic implications for the Lunigiana-Garfagnana area: Boll. Geofis. Teor. Appl., v. 55, p. 739-754.

Evans, M. A., and Battles, D.A., 1999, Fluid inclusion and stable isotope analyses of veins from the central Appalachian Valley and Ridge province: Implications for regional synorogenic hydrologic structure and fluid migration: Geological Society of America Bulletin, v. 111, p. 1841-1860.

Faulkner, D.R., and Rutter, E.H., 2001, Can the maintenance of overpressured fluids in large strike-slip fault zones explain their apparent weakness?: Geology, v. 29 (6), p. 503-506.

Faulkner, D., Jackson, C., Lunn, R., Schlische, R., Shipton, Z., Wibberley, C., and Withjack, M., 2010, A review of recent developments concerning the structure, mechanics and fluid flow properties of fault zones: J. Struct. Geol. v. 32, p. 1557-1575. http://dx.doi.org/10.1016/j.jsg.2010.06.009.

Federici, P.R., 1978, La tettonica recente dell'appennino; 2) Il bacino fluvio-lacustre di Pontremoli (Alta Val di Magra) e sue implicazioni neotettoniche: G.S.Q.P., Quaderno n. 4, p. 121-131.

Federici, P.R., 1981, Nuovi resti di vertebrato nel bacino fluvio-lacustre villafranchiano di Pontremoli (Val di Magra): Bolletino della Museo Storia Naturale della Lunigiana, 1 (2), p. 71-74.

Fellin, M.G., Reiners, P.W., Brandon, M.T., Wüthrich, E., Balestrieri, M.L., and Molli, G., 2007, Thermochronologic evidence for the exhumational history of the Alpi Apuane metamorphic core complex, Northern Apennines, Italy: Tectonics, v. 26, TC6015, doi: 10 .1029/2006TC002085.

Ferrill, D.A., Morris A.P., Sims D.W., Waiting D.J., and Hasegawa S., 2004a, Development of synthetic layer dip adjacent to normal faults, In: Sorkhabi R., Tsuji Y. (Eds.), Faults, Fluid Flow, and Petroleum Traps American Association of Petroleum Geologists Memoir. American Association of Petroleum Geologists, Tulsa, OK, USA, p. 125–138.

Ferrill, D.A., Morris, A.P., Evans, M.A., Burkhard, M., Groshong, R.H., and Onasch, C.M., 2004b, Calcite twin morphology: a low-temperature deformation geothermometer: Journal of Structural Geology, v. 26, p. 1521–1529.

Fisher, D.M., Brantley, S.L., Everett, M., and Dzvonik, J., 1995, Cyclic fluid-flow through a regionally extensive fracture network within the Kodiak accretionary prism: Journal of Geophysical Research, Solid Earth, v. 100 (B7), p. 12881-12894.

Fondriest, M., Smith, S.A.F., Candela, T., Nielsen, S.B., Mair, K., and Di Toro, G., 2013, Mirror-like faults and power dissipation during earthquakes: Geology, v. 41 (11), p. 1175-1178.

Fossen, H., Schultz, R.A., Shipton, Z.K., and Mair, K., 2007, Deformation bands in sandstone: a review: Journal of the Geological Society, v. 164, p. 755-769.

Fossen, H., 2010, Structural Geology, 463 pp., Cambridge Univ. Press, Cambridge, U. K.

Franceschelli, M., Leoni, L., Memmi, I., and Puxeddu, M., 1986, Regional distribution of Al-silicates and metamorphic zonation in the low-grade Verrucano metasediments from the Northern Apennines, Italy: Journal of Metamorphic Geology, v. 4, p. 309–321.

Frepoli, A., and Amato, A., 1997, Contemporaneous extension and compression in the Northern Apennines from earthquake fault-plane solutions: Geophys. J. Int., v. 129, p. 368-388.

Friedman, I., and O'Neil, J.R., 1977, Compilation of stable isotope fractionation factors of geochemical interest, In: Fleisher, M., ed., Data of Geochemistry (6th ed.): U.S. Geological Survey Professional Paper 440-KK, 117 p.

Ghelardoni, R., 1965, Osservazioni sulla tettonica trasversale dell'Appennino settentrionale: Boll. Soc. Geol. It., 84, pp. 276-290.

Ghibaudo, G., 1980, Deep-sea fan deposits in the Macigno Formation (middle-upper Oligocene) of the Gordana Valley, northern Apennines, Italy: Journal of Sedimentary Research, v. 50, p. 723-741.

Gianelli, G., Ruggieri, G., and Mussi, M., 1997, Isotopic and fluid inclusion study of hydrothermal and metamorphic carbonates in the Larderello geothermal field and surrounding areas, Italy: Geothermics, v. 26, p. 393-417.

Giglia, G., 1974, L'insieme Corsica-Sardegna e I suoi rapport con l'Appenino settentrionale: rassegna di dati cronologici e strutturali, *in* Maxia, C., and Pomesano A., eds., Paleogeografia del Terziario sardo nell'ambito del Mediterraneo occidentale: Cagliari, Italy, Rendiconti Semestrali della Facoltà di Scienze, Università di Cagliari, 43, p. 245–275.

Giustini, F., Brilli, M., and Patera, A., 2016, Mapping oxygen stable isotopes of precipitation in Italy: Journal of Hydrology: Regional Studies, v. 8, p. 162-181.

Goldstein, R.H., and Reynolds, J., 1994, Systematics of Fluid Inclusions in Diagenetic Minerals: Short Course Notes: Tulsa, Oklahoma, USA, The Society for Sedimentary Geology, v. 31, https:// doi .org /10 .2110 /scn .94 .31.

Gratier, J.P., Favreau, P., Renard, F., and Pili, E., 2002, Fluid pressure evolution during the earthquake cycle controlled by fluid flow and pressure-solution crack sealing, Earth Planets Space, v. 54, p. 1139-1146.

Hardy, S., and Ford, M., 1997, Numerical modelling of trishear fault propagation folding: Tectonics, v. 16, n. 5, pp. 841-854.

Hardy, S., and McClay, K., 1999, Kinematic modeling of extensional faultpropagation folding: Journal of Structural Geology, v. 21, p. 695–702.

Hilgers, C., and Urai, J.L., 2002, Experimental study of syntaxial vein growth during lateral fluid flow in transmitted light: first results: Journal of Structural Geology, v. 24, p. 1029-1043.

Hoefs, J., 1997, Stable Isotope Geochemistry: Springer-Verlag, Berlin, Germany, 200 p.

Holland, M., and Urai, J.L., 2010, Evolution of anastomosing crack-seal vein networks in limestones: insights from an exhumed high pressure cell, Jabal Shams, Oman Mountains: Journal of Structural Geology, v. 32, p. 1279-1290.

Honlet, R., Gasparrini, M., Jager, H., Muchez, P., and Swennen, R., 2017, Precursor and ambient rock paleothermometry to assess the thermicity of burial dolomitization in the southern Cantabrian Zone (northern Spain): International Journal of Earth Sciences, v. 106-7, p. 1-21.

Huber, M., Halas, S., and Sikorska, M., 2007, Evolution of prehnite-albite-calcite veins in metamorphic rocks from the Lapland Granulite Belt (Kandalaksha region of Kola Peninsula): Geologija, v. 57, p. 1-7.

Ingebritsen, S.E., and Manning, C.E., 2010, Permeability of the continental crust: Dynamic variations inferred from seismicity and metamorphism: Geofluids, v. 10, p. 193–205.

Jessell, M.W., Willman, C.E., and Gray, D.R., 1994, Bedding parallel veins and their relationship to folding: Journal of Structural Geology, v. 16, p. 753-767.

Jin, G., and Groshong, Jr. R.H., 2006, Trishear kinematic modelling of extensional fault-propagation folding: Journal of Structural Geology, v. 28, p. 170-183.

Jolivet, L., Faccenna, C., Goffé, B., Mattei, M., Rossetti, F., Brunet, C., Storti, F., Funiciello, R., Cadet, J.P., D'Agostino, N., and Parra, T., 1998, Midcrustal shear zones in postorogenic extension: Example from the northern Tyrrhenian Sea: Journal of Geophysical Research, v. 103, p. 12,123–12,160.

Ketcham, R.A., Donelick, R.A., and Carlson, W.D., 1999, Variability of apatite fission-track annealing kinetics: III. Extrapolation to geological time scales: American mineralogist, v. 84, p. 1235-1255.

Kim, Y.S., Peacock, D.C.P., and Sanderson, D.J., 2004, Fault damage zones: Journal of Structural Geology, v. 26 (3), p. 503-517.

Knott, S.D., Beach, A., Brockbank, P.J., Brown, J.L., McCallum, J.E., and Welbon, A.I., 1996, Spatial and mechanical controls on normal fault population: Journal of Structural Geology, v. 18, p. 359- 372.

Koehn, D., and Passchier, C.W., 2000, Shear sense indicators in striped bedding-veins: Journal of Structural Geology, v. 22, p. 1141-1151.

Laurent, D., Lopez, M., Chauvet, A., Sauvage, A.C., Buatier, M., and Spangenberg, J.E., 2017, Sedimentary fluids/fault interaction during syn-rift burial of the Lodève Permian Basin (Hérault, France): An example of seismic-valve mechanism in active extensional faults: Marine and Petroleum Geology, v. 88, p. 303-328.

Lockner, D.A., Byerlee, J.D., Kuksenk, V., Ponomarev, A., and Sidorin, A., 1992, Observation of quasistatic fault growth from acoustic emissions, In: Fault mechanics and transport properties of rocks, edited by Evans B. and Wong T.F., p. 3-32, Academic, San Diego, California.

Longinelli, A., Selmo, E., 2003, Isotopic composition of precipitation in Italy: a first overall map: Journal of Hydrology, v. 270, p. 75–88.

Malinverno, A., and Ryan, W.B.F., 1986, Extension in the Tyrrhenian Sea and shortening in the Apennines as result of arc migration driven by sinking of the lithosphere: Tectonics, v. 5, p. 227-245.

Mamadou, M.M., Chatelineau, M., Bourdelle, F., Boiron, M-C., Elmaleh, A., and Brouand, M., 2016, Hot fluid flows around a major fault identified by paleothermometric studies (Tim Mersoi Basin, Niger): Journal of Sedimentary Research, v. 86, p. 914-928.

Martini, I.P., Sagri, M., and Colella, A., 2001, Neogene-Quaternary basins of the inner Apennines and Calabrian arc, In: Anatomy of an orogeny: The Apennines and adjacent Mediterranean Basins, edited by Vai G.B. and Martini I.P., p. 375-400, Kluwer Acad., Dordrecht, Netherlands.

Mazzarini, F., Isola, I., Ruggieri, G., and Boschi, C., 2010, Fluid circulation in the upper brittle crust: Thickness distribution, hydraulic transmissivity fluid inclusion and isotopic data of veins hosted in the Oligocene sandstones of the Macigno Formation in southern Tuscany, Italy: Tectonophysics, v. 493, p. 118-138.

McCaig, A.M., 1988, Deep fluid circulation in fault zones: Geology, v. 16, p. 867-870.

McCrea, J.M., 1950, On the isotopic chemistry of carbonates and a paleotemperature scale: J. Chem. Phys., v. 18, pp. 849-857.

Merriman, R.J., and Frey, M., 1999, Patterns of very low-grade metamorphism in metapelitic rocks. In: Frey, M., Robinson, D. (Eds.), Low-grade Metamorphism. Blackwell Science, Oxford, pp. 61–107.

Milliken, K.L., McBride, E.F., Cavazza, W., Cibin, U., Fontana, D., Picard, M.D., and Zuffa, G.G., 1998, Geochemical history of calcite precipitation in Tertiary sandstones, Northern Apennines, Italy, *in* Morad, S., ed., Carbonate Cementation in Sandstones: International Association of Sedimentologists Special Publications, v. 26, p. 213-239.

Molli, G., Conti, P., Giorgetti, G., Meccheri, M., and Oesterling, N., 2000a, Microfabric study on the deformational and thermal history of the Alpi Apuane marbles (Carrara marbles), Italy: Journal of Structural Geology, v. 22, p. 1809–1825.

Molli, G., Giorgetti, G., and Meccheri, M., 2000b, Structural and petrological constraints on the tectono-metamorphic evolution of the Massa unit (Alpi Apuane, NW Tuscany, Italy): Geological Journal, v. 35, p. 251–264.

Molli, G., Giorgetti, G., and Meccheri M., 2002, Tectono-metamorphic evolution of the Alpi Apuane metamorphic complex. New data and constraints for geodynamic models: Boll. Soc. Geol. It., Special Issue, v. 1, p. 801–817.

Molli, G., 2008, Northern Apennine-Corsica orogenic system: an updated review, In: Siegesmund S., Fugenschuh B., Froitzheim N. (Eds.), Tectonic Aspects of the Alpine-Dinaride-Carpathian System: Geological Society of London Special Publication, v. 298, p. 413–442.

Molli, G., White, J.C., Kennedy, L., and Taini, V., 2011, Low-temperature deformation of limestone, Isola Palmaria, northern Apennine, Italy—the role of primary textures, precursory veins and intracrystalline deformation in localization: Journal of Structural Geology, v. 33, p. 255–270, https:// doi .org /10 .1016 /j .jsg .2010 .11 .015 .

Molli, G., Carlini, M., Vescovi, P., Artoni, A., Balsamo, F., Camurri, F., Clemenzi, L., Storti, F., and Torelli, L., 2018, Neogene 3-D structural architecture of the north-west Apennines: The role of the low-angle normal faults and basement thrusts: Tectonics, https:// doi .org /10 .1029 /2018TC005057, (in press).

Mongelli, F., Zito, G., Della Vedova, B., Pellis, G., Squarci, P., and Taffi, L., 1991, Geothermal regime of Italy and surrounding areas, In: V. Cermàk and L. Rybach (Editors), Terrestrial Heat Flow and the Lithosphere structure, Springer, Berlin, Germany, p. 381-394.

Montanari, L., and Rossi, M., 1982, Evoluzione delle unità stratigrafico-strutturali terziarie del nordappennino; 1. L'unità di Canetolo: Boll. Soc. Geol. It., v. 101, p. 275-289.

Montomoli, C., 2002, Vein development and fluid inclusion data: Insight on the evolution of the Tuscan Nappe in the Northern Apennine: Boll. della Soc. Geol. It., v. 1, Special Issue, p. 801–817.

Montomoli, C., Ruggieri, G., Boiron, M.C., and Cathelineau, M., 2001, Pressure fluctuation during uplift of the Northern Apennines (Italy): A fluid inclusions study: Tectonophysics, v. 341, p. 121-139.

Muchez, P., Slobodnik, M., Viaene, W.A., and Keppens, E., 1995, Geochemical constraints on the origin and migration of palaeofluids at the northern margin of the Variscan foreland, southern Belgium: Sedimentary Geology, v. 96, p. 191-200.

Mullis, J., 1979, The system methane-water as a geological thermometer and barometer from the external part of the Central Alps: Bulletin de Mineralogie, v. 102, p. 526–536.

Mullis, J., 1987, Fluid inclusion studies during very low-grade metamorphism, In: Frey, M. (Ed.), Low Temperature Metamorphism, Blackie, Glasgow, Scotland, p. 162– 199.

Mullis, J., 1988, Rapid subsidence and upthrusting in the Northern Apennines, deduced by fluid inclusion studies in quartz crystals from Porretta Terme: Schweizerische Mineralogische und Petrographische Mitteilungen, v. 68, p. 157–170.

Nesbitt, B.E., and Muehlenbachs, K., 1989, Origins and movement of fluids during deformation and metamorphism in the Canadian Cordillera: Science, v. 245, p. 733-736.

Okamoto, A., and Sekine, K., 2011, Textures of syntaxial quartz veins synthesized by hydrothermal experiments: Journal of Structural Geology, v. 33, p. 1764-1775.

Oliver, N.H.S., 1996, Review and classification of structural controls on fluid flow during regional metamorphism: Journal of Metamorphic Geology, v. 14, p. 477-492.

Oliver, N.H.S., and Bons, P.D., 2001, Mechanisms of fluid flow and fluid-rock interaction in fossil metamorphic hydrothermal systems inferred from vein-wallrock patterns, geometry and microstructure: Geofluids v. 1, 137-162.

Oncken, O., 1982, Basin reconstruction by coalification studies: Geol. Rundsch., 71, 579–602.

O'Neil, J.R., Clayton, R.N., and Mayeda, T.K., 1969, Oxygen isotope fractionation in divalent metal carbonates: The Journal of Chemical Physics, v. 51, p. 5547–5558, https:// doi .org /10 .1063 /1 .1671982 .

Parry, W.T., and Bruhn, R.L., 1987, Fluid inclusion evidence for a minimum 11 km vertical offset on the Wasatch fault, Utah: Geology, v. 15, p. 67-70.

Parry, W.T., 1998, Fault-fluid compositions from fluid inclusion observations and solubilities of fracture-sealing minerals: Tectonophysics, v. 290, p. 1-26.

Passchier, C.W., and Trouw, R.A.J., 2005, Microtectonics, second ed., Springer Verlag, Berlin, Germany, 371 p.

Patacca, E., Sartori, R., and Scandone, P., 1990, Tyrrhenian Basin and Apenninic arc: Kinematic relations since late Tortonian times: Mem. Soc. Geol. It., v. 45, p. 425–451.

Petsch, S.T., Berner, R.A., and Eglinton, T.I., 2000, A field study of the chemical weathering of ancient sedimentary organic matter: Organic Geochemistry, v. 31, p. 475–487.

Phillips, W.J., 1972, Hydraulic fracturing and mineralization: Jour. Geol. Soc. Lond., v. 128, p. 337-359.

Plesi, G., 1975, La nappe de Canetolo: Bull. Soc. Géol. Fr., v. 6, p. 979-983.

Principi, G., and Treves, B., 1984, Il sistema corso-appennino come prisma d'accrezione. Riflessi sul problema generale del limite Alpi-Appennino: Mem. Soc. Geol. lt., v. 28, p. 529-576.

Raggi, G., 1985, Neotettonica ed evoluzione paleogeografica plio-pleistocenica del Bacino de fiume Magra: Mem. Soc. Geol. It., v. 30, p. 35-62.

Ramsay, J.G., 1980, The crack-seal mechanism of rock deformation: Nature, v. 284, p. 135-139.

Ramsay, J.G., and Huber, M.I., 1983, The Techniques of Modern Structural Geology: Volume I: Strain Analysis: London, UK, Academic Press, 307 p.

Reches, Z., and Lockner, D.A., 1994, Nucleation and growth of faults in brittle rocks: Journal of Geophysical Research, v. 99, n. B9, p. 18,159-18,173.

Renard, F., Gratier, J.P., and Jamtveit, B., 2000, Kinetics of crack-sealing, intergranular pressure solution, and compaction around active faults: Journal of Structural Geology, v. 22 (10), p. 1395-1407.

Reutter, K.J., Teichmuller, M., Teichmuller, R., and Zanzucchi, G., 1981, Le ricerche sulla carbonificazione dei frustoli vegetali nelle rocce clastiche, come contributo ai problemi di paleogeotermia e tettonica nell'Appenino settentrionale: Mem. Soc. Geol. It., v. 21, p. 111-126.

Robert, F., Boullier, A.-M., and Firdaous, K., 1995, Gold-quartz veins in metamorphic terranes and their bearing on the role of fluids in faulting: Journal of Geophysical Research, v. 100, p. 12,861-12,879.

Roedder, E., 1984, Fluid inclusions, *in* Ribbe, P.H., ed., Reviews in Mineralogy: Washington, D.C., USA, Mineralogical Society of America, v. 12, 644 p.

Roure, F., Swennen, R., Schneider, F., Faure, J.L., Ferket, H., Guilhaumou, N., Osadetz, K., Robion, P., and Vandeginste, V., 2005, Incidence and importance of tectonics and natural fluid migration on reservoir evolution in foreland fold-and-thrust belts: In: Brosse, E. (Ed.), Oil and Gas Science and Technology. Revue de l'IFP 60, pp. 67–106.

Royden, L., 1988, Flexural behaviour of the continental lithosphere in Italy: Constraints imposed by gravity and deflection data: Journal of Geophysical Research, v. 93, p. 7747–7766.

Salvini, F., 2017, Daisy 3: The Structural Data Integrated System Analyzer. Software: Rome, Italy, Roma Tre University, GeoQuTe Lab, http://host.uniroma3.it/progetti/fralab/.

Schito, A., Andreucci, B., Aldega, L., Corrado, S., Di Paolo, L., Zattin, M., Szaniawski, R., Jankowski, L., and Mazzoli, S., 2018, Burial and exhumation of the western border of the Ukrainian Shield (Podolia): a multi-disciplinary approach: Basin Research, 30, (Suppl. 1), p. 532–549.

Schlische, R.W., 1995, Geometry and origin of fault-related folds in extensional settings: American Association of Petroleum Geologists Bulletin, v. 79, p. 1661–1678.

Sclater, J.G., and Christie, P., 1980, Continental stretching: an explanation of the post-mid cretaceous subsidence of the central North Sea basin: J. Geophys. Res. Solid Earth, 85 (B7), 3711–3739.

Serri, G., Innocenti, F., and Manetti, P., 1993, Geochemical and petrological evidence of the subduction of delaminated Adriatic continental lithosphere in the genesis of the Neogene-Quaternary magmatsim of central Italy: Tectonophysics, v. 223, p. 117-147.

Sibson, R.H., Moore, J.McM., and Rankin, A.H., 1975, Seismic pumping-a hydrothermal fluid transport mechanism: Jour. Geol. Soc. Lond., v. 131, p. 653-659.

Sibson, R.H., Robert, F., and Poulsen, K.H., 1988, High-angle reverse faults, fluid-pressure cycling, and mesothermal gold-quartz deposits: Geology, v. 16, p. 551-555.

Sibson, R.H., 1996, Structural Permeability of fluid-driven fault-fracture meshes: Journal of Structural Geology, v. 18, p. 1031-1042.

Sibson, R.H., 2000, Fluid involvement in normal faulting: Journal of Geodynamics, v. 29, p. 469-499.

Sibson, R.H., 2004, Controls on maximum fluid overpressure defining conditions for mesozonal mineralization: Journal of Structural Geology, v. 26, p. 1127–1136, https:// doi .org /10 .1016 /j .jsg .2003 .11 .003.

Smeraglia, L., Billi, A., Carminati, E., Cavallo, A., and Doglioni, C., 2017, Field- to nano-scale evidence for weakening mechanisms along the fault of the 2016 Amatrice and Norcia earthquakes, Italy: Tectonophysics, v. 712-713, p. 156-169.

Smith, S.A.F., Billi, A., Di Toro, G., and Spiess, R., 2011, Principal slip zones in limestone: Microstructural characterization and implications for the seismic cycle (Tre Monti fault, Central Apennines, Italy): Pure and Applied Geophysics, v. 168, p. 1-27, doi:10.1007/s00024-011-0267-5.

Solum, J.G., and Huisman, B.A.H., 2016, Toward the creation of models to predict static and dynamic fault-seal potential in carbonates: Petroleum Geoscience, v. 23 (1), p. 70-91.

Storti, F., 1995, Tectonics of the Punta Bianca promontory: Insights for the evolution of the Northern Apennines-Northern Tyrrhenian Sea basin: Tectonics, v. 14, p. 832–847.

Teichmüller, M., and Teichmüller, R., 1967, Diagenesis of coal (coalification), In: Diagenesis in Sediments by Larsen G. and Chilingar G.V. Edn., Developments in Sedimentology, Elsevier, v. 8, p. 391-415.

Teichmüller, M., 1987, Organic material and very low grade metamorphism, In: Frey M. (Ed.), Low-temperature Metamorphism, Chapman and Hall, Glasgow, Scotland, p. 114-161.

Thomson, S.N., Brandon, M.T., Reiners, P.W., Zattin, M., Isaacson, P.J., and Balestrieri, M.L., 2010, Thermochronologic evidence for orogeny-parallel variability in wedge kinematics during extending convergent orogenesis of the Northern Apennines, Italy: Geol. Soc. Am. Bull., v. 122, p. 1160-1179.

Tissot, B.P., and Welte, D.H., 1984, From Kerogen to Petroleum, In: Petroleum Formation and Occurrence, Springer, Berlin Heidelberg, Germany, p. 160-198.

Torabi, A., and Berg, S.S., 2011, Scaling of fault attributes: a review: Marine and Petroleum Geology, v. 28, p. 1444–1460, http://dx.doi.org/10.1016/j.marpetgeo.2011.04.003.

Vandeginste, V., Swennen, R., Allaeys, M., Ellam, R.M., Osadetz, K., and Roure, F., 2012, Challenges of structural diagenesis in foreland fold-and-thrust belts: a case study on paleofluid flow in the Canadian Rocky Mountains west of Calgary: Mar. Petrol. Geol., v. 35, p. 235-251.

Veizer, J., Ala, D., Azmy, K., Bruckschen, P., Buhl, D., Bruhn, F., Carden, G.A.F., Diener, A., Ebneth, S., Godderis, Y., Jasper, T., Korte, C., Pawellek, F., Podlaha, O.G., and Strauss, H., 1999, $^{87}Sr/^{86}Sr$, $\delta^{13}C$ and $\delta^{18}O$ evolution of Phanerozoic seawater: Chemical Geology, v. 161, p. 59-88.

Vermilye, J.M., and Scholz, C.H., 1998, The process zone: A microstructural view of fault growth: Journal of Geophysical Research, v. 103, n. B6, p. 12,223-12,237.

Vescovi, P., 1998, Le Unità Subliguri dell'alta Val Parma (Provincia di Parma): Atti Ticinesi di Scienze della Terra, v. 40, p. 215-231.

Vescovi, P., 2005, The Middle Miocene Mt. Ventasso – Mt. Cimone arcuate structure of the Emilia Apeninnes: Bollettino della Società Geologica Italiana, v. 124, p. 53-67.

Vilasi, N., Malandain, J., Barrier, L., Callot, J-P., Amrouch, K., Guilhaumou, N., Lacombe, O., Muska, K., Roure, F., and Swennen, R., 2009, From outcrop and petrographic studies to basin-scale fluid flow modelling: the use of the Albanian natural laboratory for carbonate reservoir characterisation. Tectonophysics, v. 474 (1-2), p. 367-392.

Virgo, S., Abe, S., and Urai, J.L., 2014, The evolution of crack seal vein and fracture networks in an evolving stress field: Insights from Discrete Element Models of fracture sealing: Journal of Geophysical Research, Solid Earth, v. 119, p. 8708–8727.

Walther, J.V., and Orville, P.M., 1982, Volatile production and transport in regional metamorphism: Contrib. Mineral. Petrol., v. 79, p. 252-257.

Withjack, M.O., Olson, J., and Peterson, E., 1990, Experimental models of extensional forced folds: American Association of Petroleum Geologists Bulletin, v. 74, p. 1038–1054.

Withjack, M.O., and Callaway, S., 2000, Active Normal Faulting Beneath a Salt Layer: An Experimental Study of Deformation Patterns in the Cover Sequence: American Association of Petroleum Geologists Bulletin, v. 84, n. 5, pp. 627–651.

Wüstefeld, P., Hilse, U., Lüders, V., Wemmer, K., Koherer, B., and Hilgers, C., 2017, Kilometer-scale fault-related thermal anomalies in tight gas sandstones: Marine and Petroleum Geology, v. 86, p. 288-303.

Zattin, M., Picotti, V., and Zuffa, G.G., 2002, Fission-track reconstruction of the front of the Northern Apennine thrust wedge and overlying Ligurian unit: American Journal of Science, v. 302, p. 346–379.

FIGURE CAPTIONS

Figure 1. (A) Location of the study area, in the inner part of the Northern Apennines, Italy. (B) Tectonic sketch map of the region where the Lunigiana extensional basin developed (modified from Bernini, 1997); the black and white traces indicate the geologic cross-section represented in (D) and the seismic line in Figure 2, while the black and white rectangle represents the area shown in Figure 3A. NLB—Northern Lunigiana basin; SLB—Southern Lunigiana basin. (C) Schematic column of the inner Northern Apennines stratigraphy. (D) Geological cross-section passing through the studied segment of the Compione extensional fault zone (after Bernini and Papani, 2002). OTT—Ottone Flysch Formation; MAC—Macigno Sandstones Formation; SUBL.—Subligurian Succession; m (a.s.l.)—meters above sea level.

Figure 2. (A) Depth converted seismic line and (B) line drawing highlighting the geometry of the Compione Fault, Northern Apennines, Italy, in the subsurface (segment of a seismic reflection profile acquired from Eni S.p.A.). The seismic reflection profile is depth converted with the Move Software (provided by Midland Valley Exploration Ltd.). By using the “User defined tables/checkshots” method, 13 Time/Interval Velocity tables were defined for the common mid-point (CMP) gathers (CMP1–CMP13 in A). The interval velocities derive by Dix conversion of stacking velocity used for the processing sequence as provided for this seismic profile. The Dix interval velocities are in between 3130 and 7644 m/sec, they had an overall increase down to 5 sec (two-way time) in the seismic reflection profile before depth conversion. v=h—vertical equals horizontal.

Figure 3. (A) Simplified structural map of the Northern Lunigiana, Northern Apennines, Italy, extensional basin showing the main extensional fault zones that constitute the Northern Lunigiana extensional fault system, bounding the basin to the NE. The black and white trace A–B and the rectangle refer to (B) and (C), respectively. (B) Schematic geological cross-section showing the Geometry of the extensional fault propagation fold in the footwall damage zone of the Compione

extensional fault zone, overprinting the out-of-sequence (O-of-Seq) thrust-related fold geometry. (C) Structural map of the study area showing structural and sampling sites (S).

Figure 4. (A) Geologic cross-section across the Compione fault damage zone, Northern Apennines, Italy, and stereographic projections of structural data (Schmidt lower hemisphere). The trace of the section is indicated in Figure 3C. Ex.F. c.i.—Extensional Faults contouring interval; S-s.F. c.i.—Strike-slip Faults contouring interval; FW non-tilted PZ c.i.—Footwall non-tilted Process Zone contouring interval; meters a.s.l.—meters above sea level. (B) Outcrop picture and line drawing of the hanging wall damage zone at Site 2, showing synthetic extensional faults in the Ottone Flysch Formation. (C) Outcrop picture and line drawing of the footwall damage zone at Site 4, showing the major E-W footwall splay extensional fault zone; red areas highlight the master slip surface.

Figure 5. (A) Outcrop picture and line drawing of conjugate shear veins and extensional faults in the footwall damage zone to background transition (44°19′56.65″N 10°3′41.49″E). (B) Stereographic projection of structural data in this area; dashed lines represent bedding. (C) Outcrop picture and line drawing of Site 5; dashed white line corresponds to bedding, white lines highlight conjugate shear veins and faults, and dashed black lines indicate late cataclastic faults; white (black) arrows indicate kinematics before (after) bedding rotation. (D) Stereographic projection of structural data collected at this site. (E) Detail of (C) showing a shear vein reactivated along a synthetic subsidiary fault and later crosscut along an antithetic one. (F) Slickenfibers on a synthetic subsidiary fault showing multiple slip directions; coin for scale.

Figure 6. (A) Stereographic projections (Schmidt lower hemisphere) of footwall shear veins and extensional subsidiary conjugate faults, measured at sites 4 and 5, and separated for sectors compartmentalized by late-stage large-scale cataclastic faults. In (B) data are restored to horizontal using the related bedding orientation; black (white) dots indicate normal (reverse) kinematics; reverse kinematics are apparent because of shear reactivation after bedding rotation. S—sampling sites.

Figure 7. Microphotographs of veins hosted in the footwall and hanging wall damage zones of the Compione extensional fault. (A) Prehnite (Prh) crystals overgrown by quartz (Qz) and MC1 calcite; MC2 calcite grew in dissolution fractures outlined by small dotted white lines (cross-polarized light). (B) Prh growing in columnar-radiating structures, characterized by an abrupt change in luminescence color and MC1A calcite crystals recrystallized in MC1B calcite along crystal fractures, cathodoluminescence (CL) image. (C) Vein composed of euhedral to subhedral Qz rims and MC1 replacive (rep) and rhombohedric (rho) calcite crystals in the center (cross-polarized light). (D) CL detail of (C) showing MC1A and MC1B replacing prismatic Prh crystals. (E) Stained hand sample displaying pink MC1 calcite and composed of five fracturing-sealing increments and/or shear reactivations. (F) Detail of (E) illustrating micrometric wide slip surfaces formed by coseismic slip (cross-polarized light). (G) Shear bands composed of recrystallized Qz subgrains and replacive MC1 calcite crystals (cross-polarized light). (H) Isomorphous replacement of Prh crystals by MC2 calcite (CL). (I) MC1A isomorphous replacements of prehnite crystals cut by late microfractures cemented with MC2 calcite (CL). (J) Sample near the Compione fault core showing disaggregated texture cemented by MC2 calcite. (K) Cross-polarized light image showing OC1 “dirty” and OC2 “clear” calcites textures. (L) CL image highlighting contrast in luminescence colors between OC1 and OC2 calcites from dull red to bright red and pressure solution affecting both OC1 and OC2. (M) Host rock clast in OC1 and late fractures filled by OC2 calcite and quartz (qz). (N) CL image showing detail of a bedding parallel vein where OC2 calcite, associated with qz, isomorphously replaces prehnite crystals. (O) Thin section scan of a breccia-vein composed of OC2 calcite cement collected in extensional S-C (schistosity-cisaillement) structures near the Compione fault core. MC—Macigno Sandstones Formation calcite cements; OC—Ottone Flysch Formation calcite cements.

Figure 8. Stable isotope data. (A) $\delta^{18}O$ vs. $\delta^{13}C$ plot of calcite from veins and host rocks; the dashed grey rectangle indicates the range of isotopic values of Cretaceous limestone (Lms.) (after Veizer et al., 1999) and the dashed black rectangle indicates those of Late Oligocene– Early Miocene Macigno Sandstones Formation (after Milliken et al., 1998). (B, C) Plots of $\delta^{18}O$ (B) and $\delta^{13}C$ (C) vs. distance (m) from the Compione fault core, Northern Apennines, Italy. FC—Fault core; VSMOW—Vienna standard mean ocean water; VPDB—Vienna Pee Dee belemnite. In the legend Ottone refers to calcite cements hosted in the Ottone Flysch Formation.

Figure 9. Microphotographs in plane polarized light of fluid inclusion types, in the analyzed veins. (A) Monophase gaseous inclusions Q2 cooled at –100 °C. (B) Raw spectra of Raman analysis performed on Q2 inclusions showing peaks corresponding to CH4. (C) Fluid inclusion assemblages (FIA) of Q1 aqueous biphase inclusions in quartz from a footwall vein. (D) FIA of aqueous biphase inclusions with a negative crystal shape in MC1. (E) FIA of aqueous biphase inclusions in MC2. (F) FIA of aqueous monophase inclusions in OC2, overprinting a OC1 vein, big inclusions in OC2 are biphase aqueous. MC—Macigno Sandstones Formation calcite cements; OC—Ottone Flysch Formation calcite cements.

Figure 10. Frequency distribution plots of homogenization (Thtot) and ice melting (Tmice) temperatures. (A) Thtot of Q2 monophase gaseous inclusions in quartz. (B) Thtot of biphase aqueous inclusions in footwall veins. (C) Tmice of biphase aqueous inclusions in footwall veins. (D) Thtot of biphase aqueous inclusions in hanging wall veins. (E) Tmice of monophase and biphase aqueous inclusions in hanging wall veins. Macigno Calcite—Macigno Sandstones Formation calcite cements; OC—Ottone Flysch Formation calcite cements; Footwall veins, hosted in the Macigno Sandstones Formation, from Sites 4, 5, 7, and 13 in Figures 3A and 3C; Hanging wall veins, hosted in the Ottone Flysch Formation, from Sites 2, 3, 8, 9, and 10 in Figure 3C.

Figure 11. Plot of homogenization temperatures (Thtot) vs. ice melting temperatures (Tmice) of measured fluid inclusions. Ice melting temperatures are reported along with salinity in NaCl eq.

wt%, according to Bodnar (1993). Macigno Calcite—Macigno Sandstones Formation calcite cements; Ottone Calcite—Ottone Flysch Formation calcite cements; Footwall veins, hosted in the Macigno Sandstones Formation, from Sites 4, 5, 7, and 13 in Figures 3A and 3C; Hanging wall veins, hosted in the Ottone Flysch Formation, from Sites 2, 3, 8, 9, and 10 in Figure 3C.

Figure 12. Burial and thermal history of the Macigno Sandstones Formation, Northern Apennines, Italy, shaded in grey, using a geothermal gradient of 25 °C/km up to the end of the Miocene and of 30 °C/km since the Pliocene (P.). Striped areas represent the stratigraphic range of Site 14.

Figure 13. Trishear predicted geometry of the Compione Fault, Northern Apennines, Italy, using the method of Jin and Groshong (2006). Monocline width is around twice the footwall monocline width assuming a linear velocity field in the trishear zone. Striped unit above the basement correspond to Burano Evaporites.

Figure 14. Sketch illustrating the typical paragenetic evolution of conjugate veins in the footwall of the Compione Fault, Northern Apennines, Italy. (A) Pristine crystal textures of the initial infilling event. (B) Microstructural modifications after shear reactivation. (C) After late-stage reactivation. (D) Schematic table showing the cyclic events, indicating the relative chronology of fracturing, precipitation, and dissolution processes, along with their temperature range. (E) Schematic evolution of fluid pressure, reported as ratio to lithostatic pressure, and shear stress in time relative to earthquake rupturing and to shearing, fracturing, precipitation, and dissolution processes (D) in fault-related veins. Prh—prehnite, Qz—quartz; MC—Macigno Sandstones Formation calcite cements. P—pressure; tau—shear stress; EQ— seismic rupture.

Figure 15. Data are from Sites 4, 5, 7, and 13 in the footwall damage zone (MC) and from Sites 2, 3, 8, 9, and 10 in the hanging wall damage zone (OC); see Figures 3A and 3C. (A) Isochores are plotted for the different fluid inclusion types. Peak burial derived from vitrinite reflectance modelling is used as an independent constraint to calculate a maximum trapping temperature for MC1A (shaded area). (B) Oxygen isotope fractionation during equilibrium calcite precipitation. The

fluid oxygen composition is reported as a function of calcite oxygen composition and temperature. Square symbols and error bars represent the mean value and range of footwall calcite MC1A, MC1B, and MC2. OC2 calcite is represented by the white circles. Dashed lines describe the inferred fluid evolution during time. MC—Macigno calcite cements; OC—Ottone Flysch Formation calcite cements; VR (Ro%)—Maximum burial depth estimated from vitrinite reflectance measurements; VSMOW—Vienna standard mean ocean water.

Figure 16. Phase diagrams for calcium and alumina minerals in terms of Ca2+/(H+)2 activity ratio and of aqueous SiO2 activity at 200 °C (A) and at 150 °C (B).

Figure 17. Cartoon showing the proposed evolution of the Compione Fault, Northern Apennines, Italy. (A) Onset of extensional deformations overprinting the previously stacked Sub-Ligurian and Ligurian thrust sheets onto the Macigno foredeep sandstones (MAC). A wide process zone forms, mainly consisting of conjugate shear fractures that enhance the advection of hydrothermal fluids and rapid cementation. (B) Extensional fault-propagation folding during upward fault migration, causing bending of part of the process zone closer to the prospect master shear zone and re-activation of conjugate shear veins as both synthetic and antithetic subsidiary extensional faults. (C) Shear localization, fault breakthrough and accommodation of most of the displacement in the fault core, hanging wall, and footwall subsidiary fault zones. Black arrows are formational fluids, white and black ones are high-temperature low-salinity hydrothermal fluids, white and grey ones are meteoric fluids and black and grey ones are low-temperature high-salinity fluids. OTT—Ottone Flysch Formation; Prh—prehnite, Qz—quartz; MC—Macigno calcite cement; OC—Ottone Flysch Formation calcite cements.

Table 1. Suummary of petrographic observations and stable isotope analyses results of the different carbonate cements.

Table 2. Summary of petrographic observations and microthermometry analyses results of quartz and carbonate cements.

Table 3. Summary of results of vitrinite reflectance measurements.

Figure DR1. Seismic reflection profile of Fig. 2 before being depth-converted.

Figure DR2. (A-B) Outcrop pictures of coarse sandstones strata in footwall damage zone Site 5. White dotted lines represent bedding, white lines are conjugate extensional shear veins and fractures with σ_1 orthogonal to bedding, black dashed lines are late-stage extensional shear fractures and red dashed lines indicate strike-slip shear veins and fractures. White arrows indicate pre-bedding rotation kinematics while black arrows indicate kinematics after bedding rotation. (C) Stained hand specimen of footwall fault-related shear vein; black dotted lines separate different opening events. (D) XPL image showing, as in C, multiple openings (separated by white dotted lines), of which some interested by shearing and quartz recrystallization. (E) PPL image of vein showing both MC1A and MC2 replacive calcite crystals along with quartz and rhombohedric MC1A. (F-G-H) CL images showing progressive prehnite dissolution and replacement by MC calcites.

Figure DR3. Fluid inclusion assemblage in quartz of footwall damage zone fault-related shear veins showing aqueous inclusion (white), gaseous CH4 inclusions (black) and an inclusion containing liquid H2O and gaseous CH4 (black and white). In (A) at 20 °C and in (B) at -100 °C.

[1]GSA Data Repository item 2018xxx, including structural sites and samples list, and stable isotopic, microthermometric and SEM-EDS analyses results, is available online at www.geosociety.org/pubs/ft20XX.htm, or on request from editing@geosociety.org or Documents Secretary, GSA, P.O. Box 9140, Boulder, CO 80301, USA.

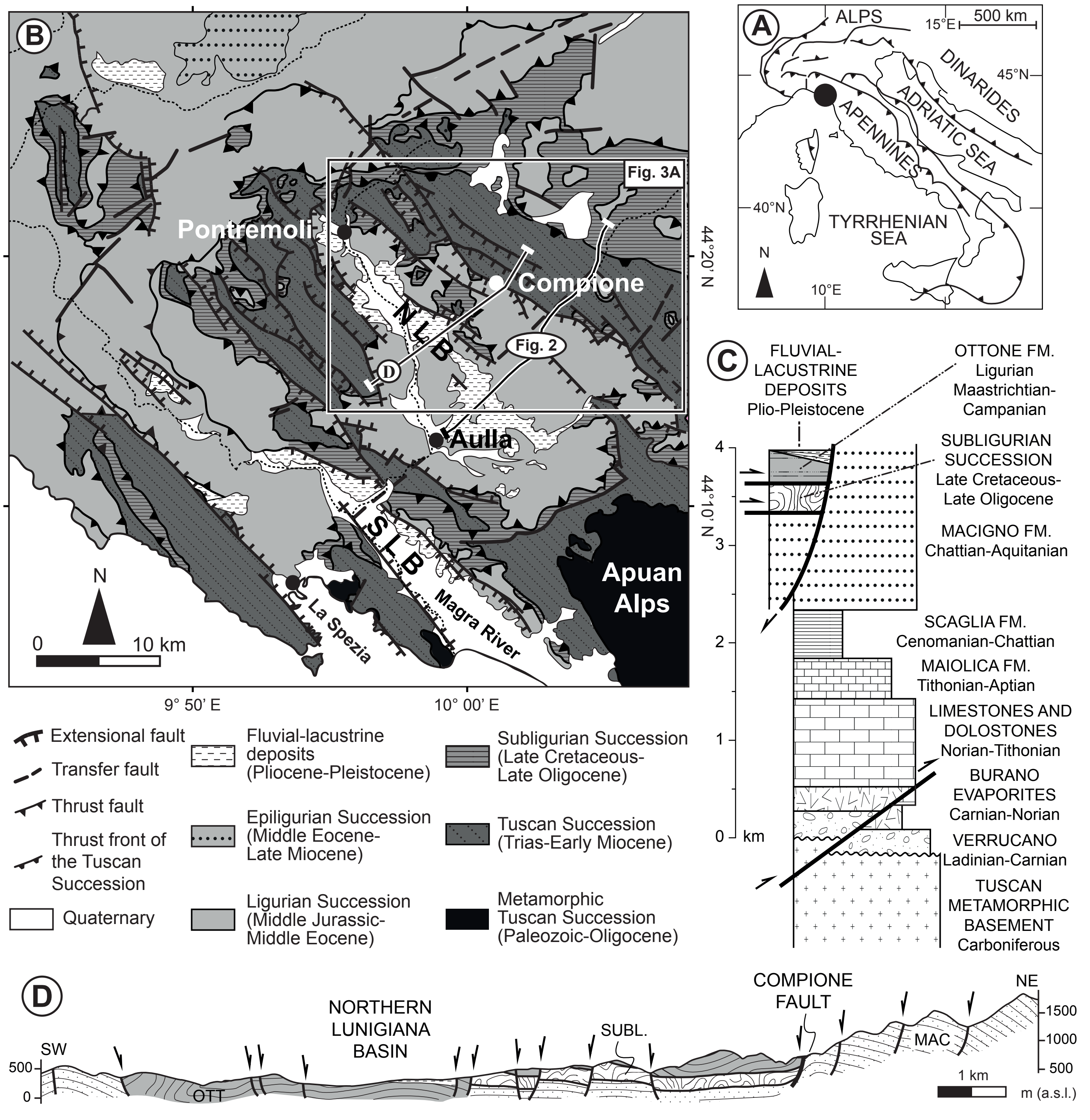

Lucca et al.
Fig. 1

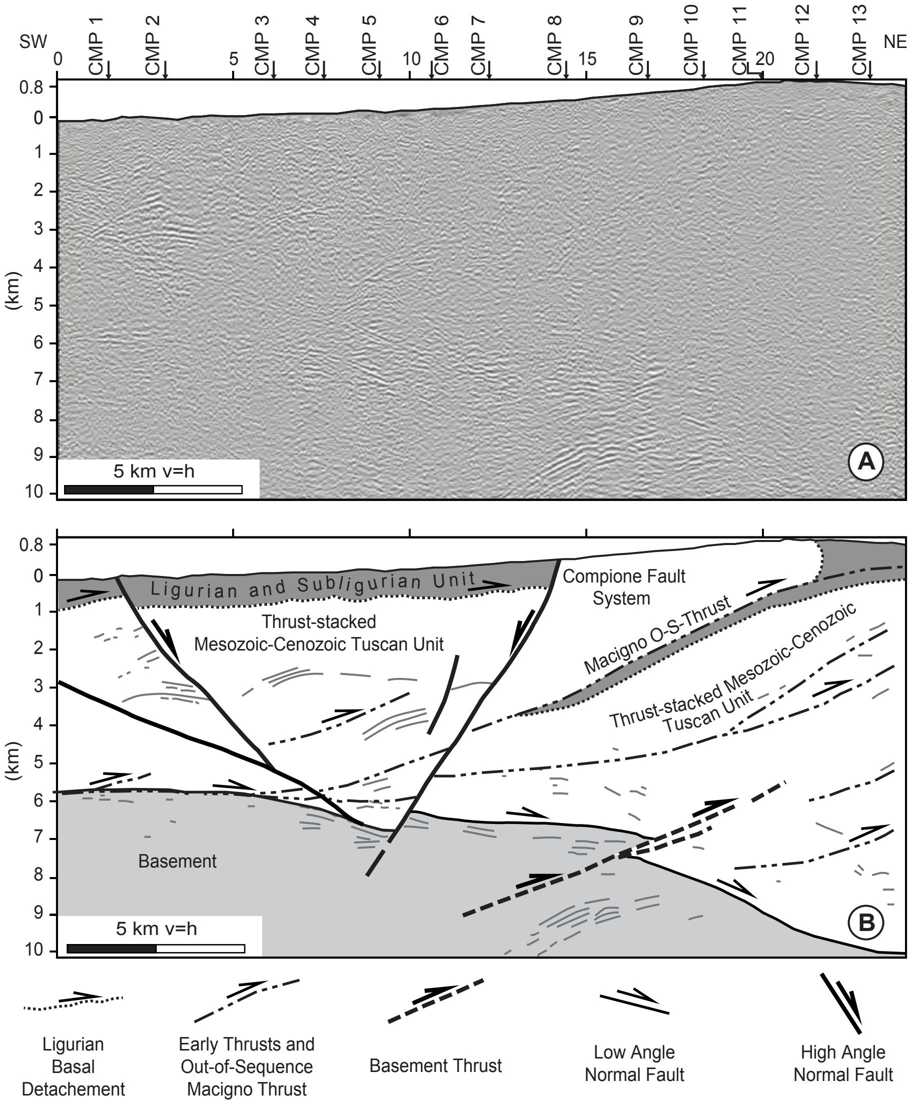

Lucca et al.
Fig. 2

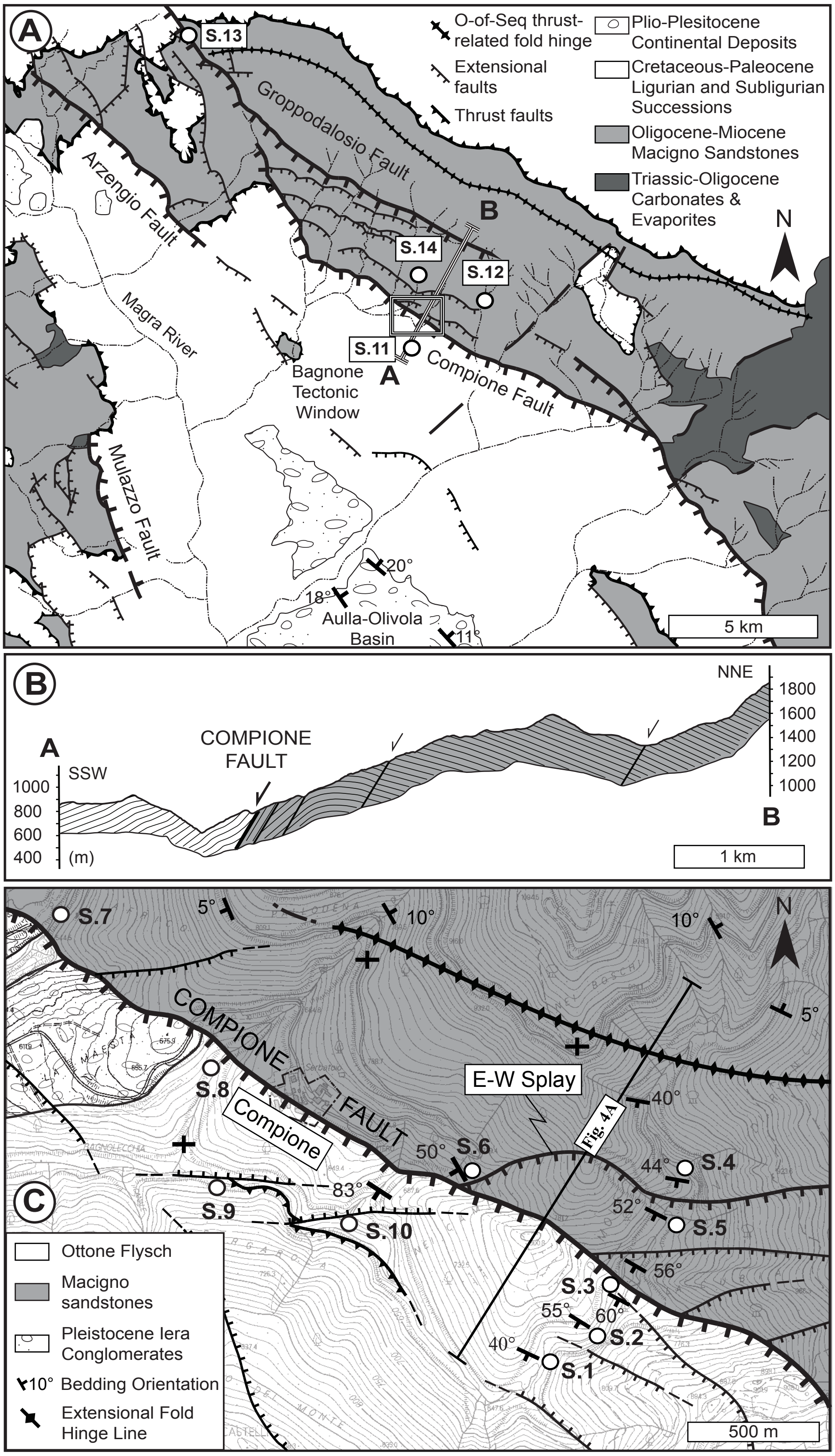

Lucca et al.
Fig. 3

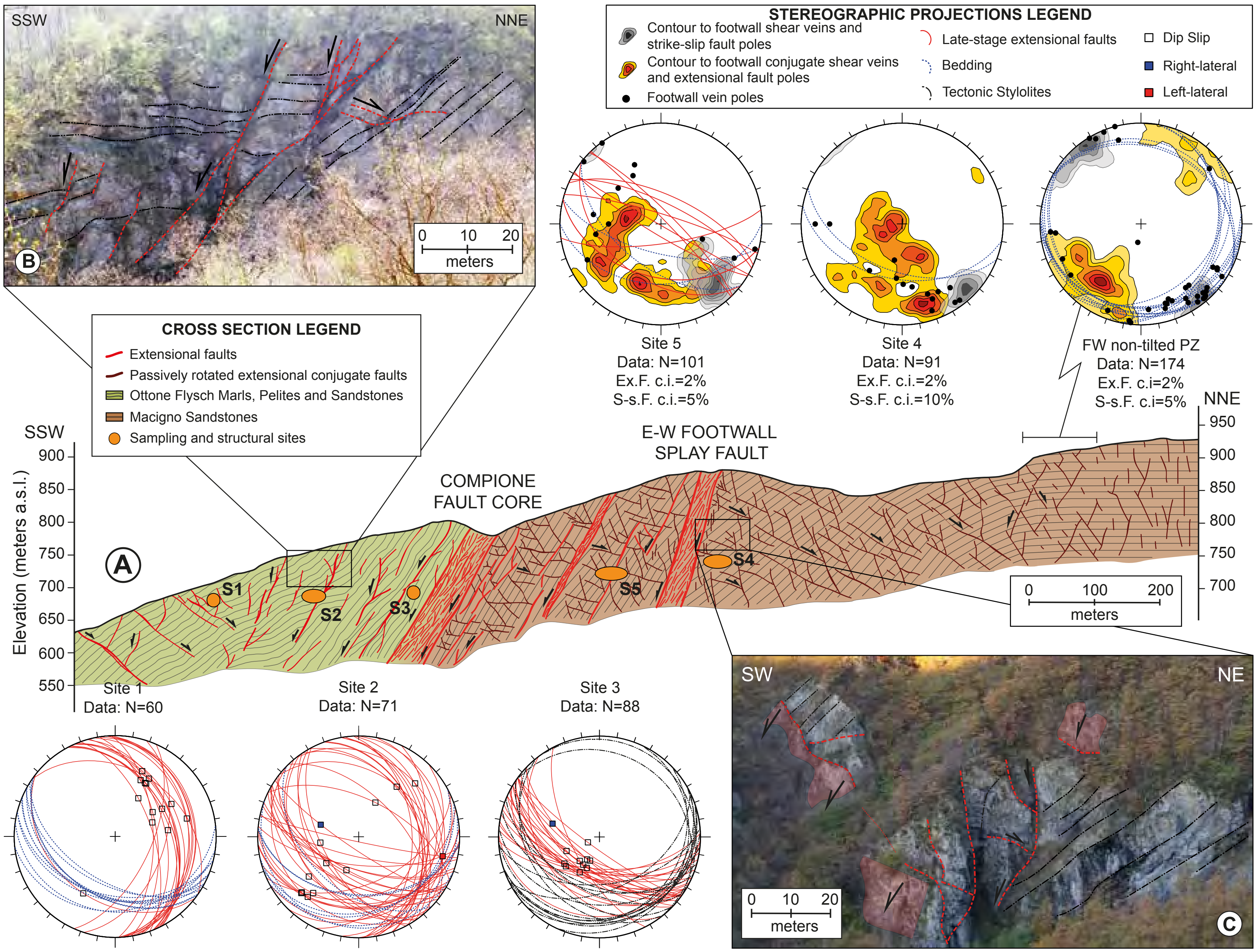

Lucca et al.

Fig. 4

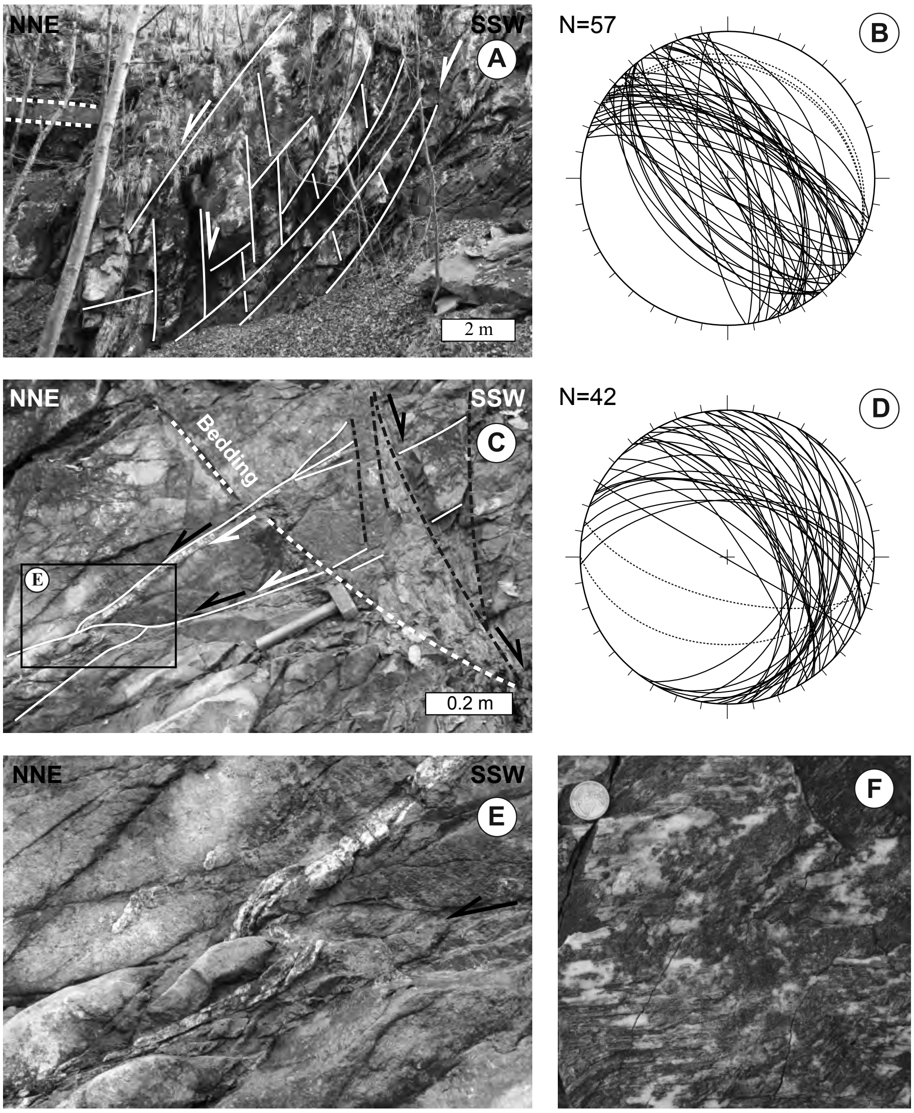

Lucca et al.
Fig. 5

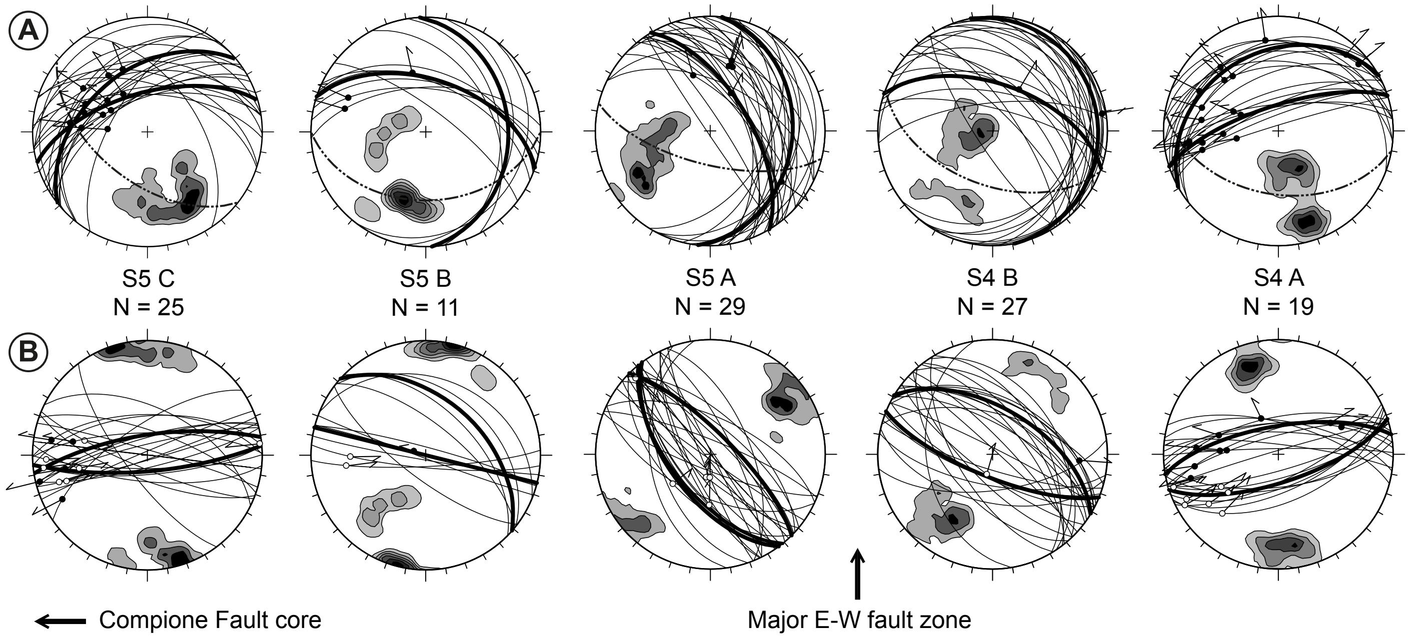

Lucca et al.
Fig. 6

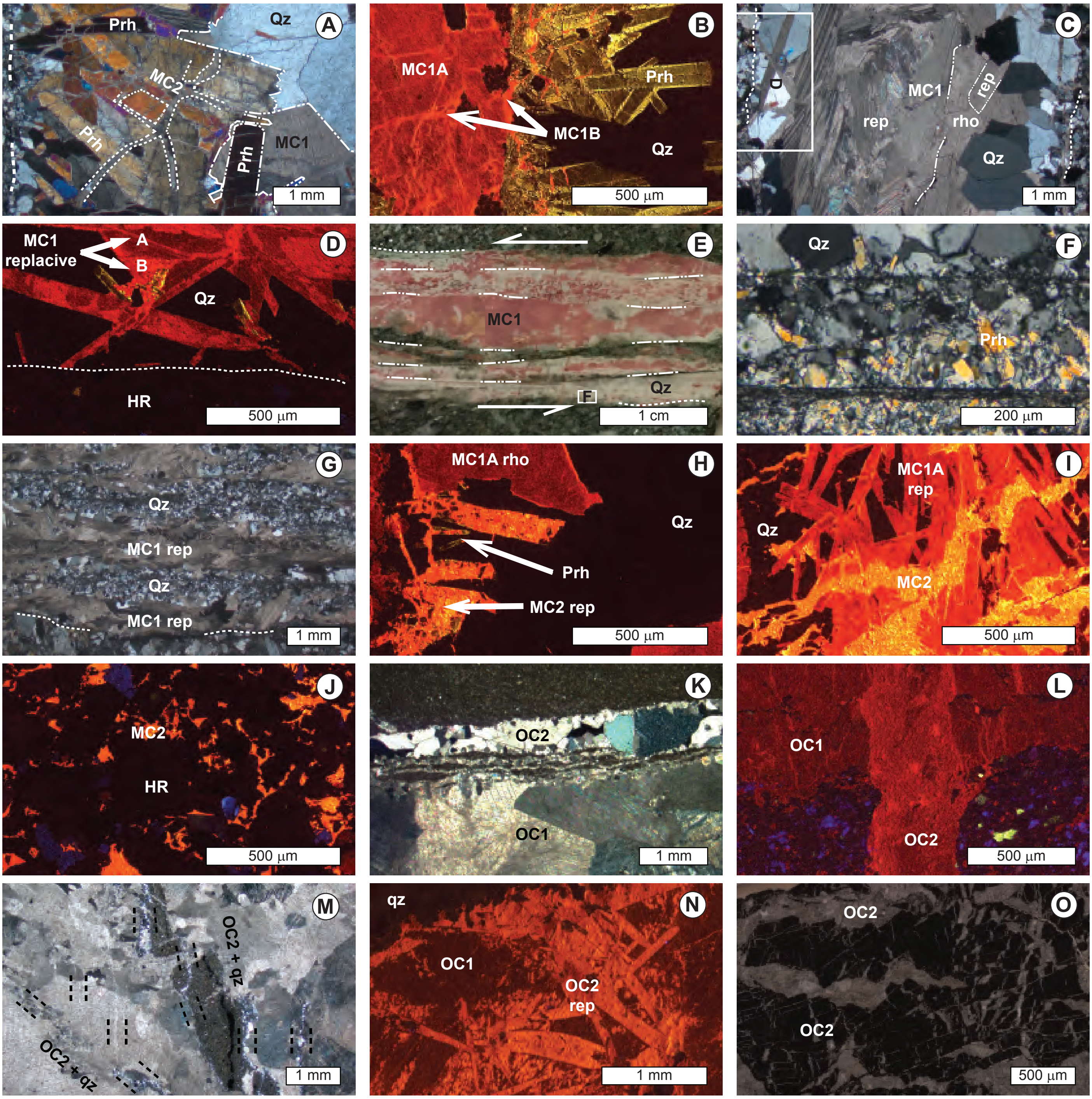

Lucca et al.
Fig. 7

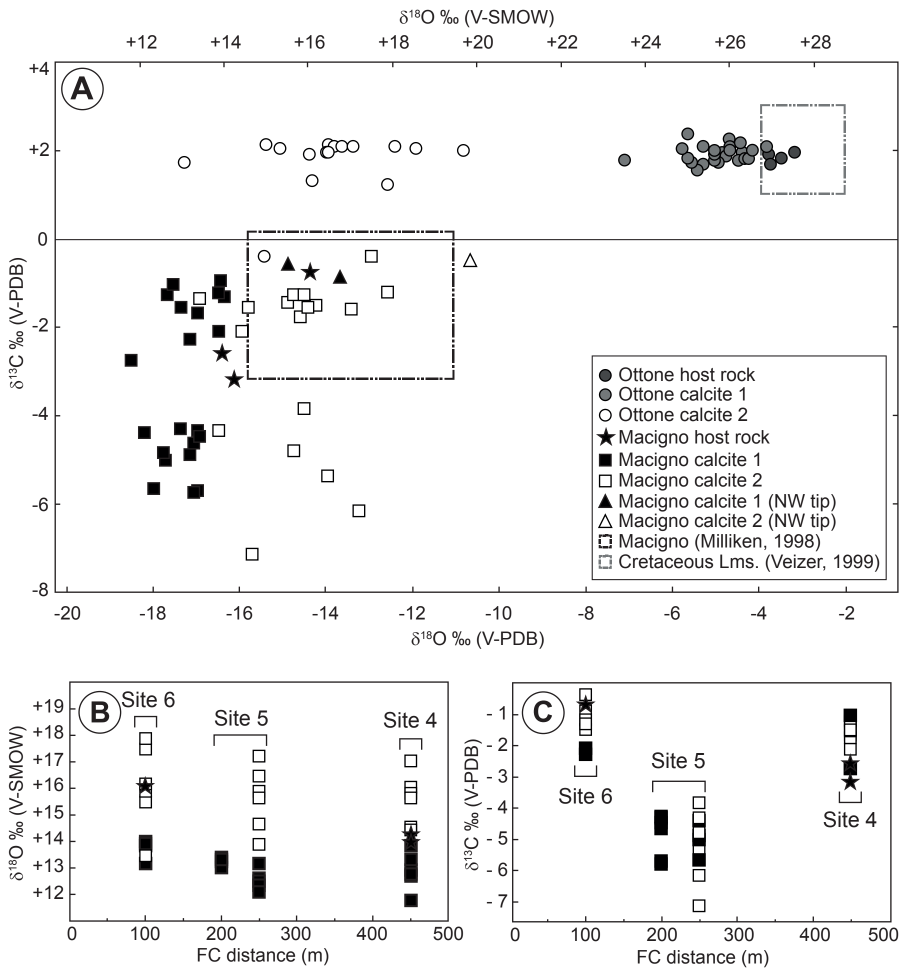

Lucca et al.
Fig. 8

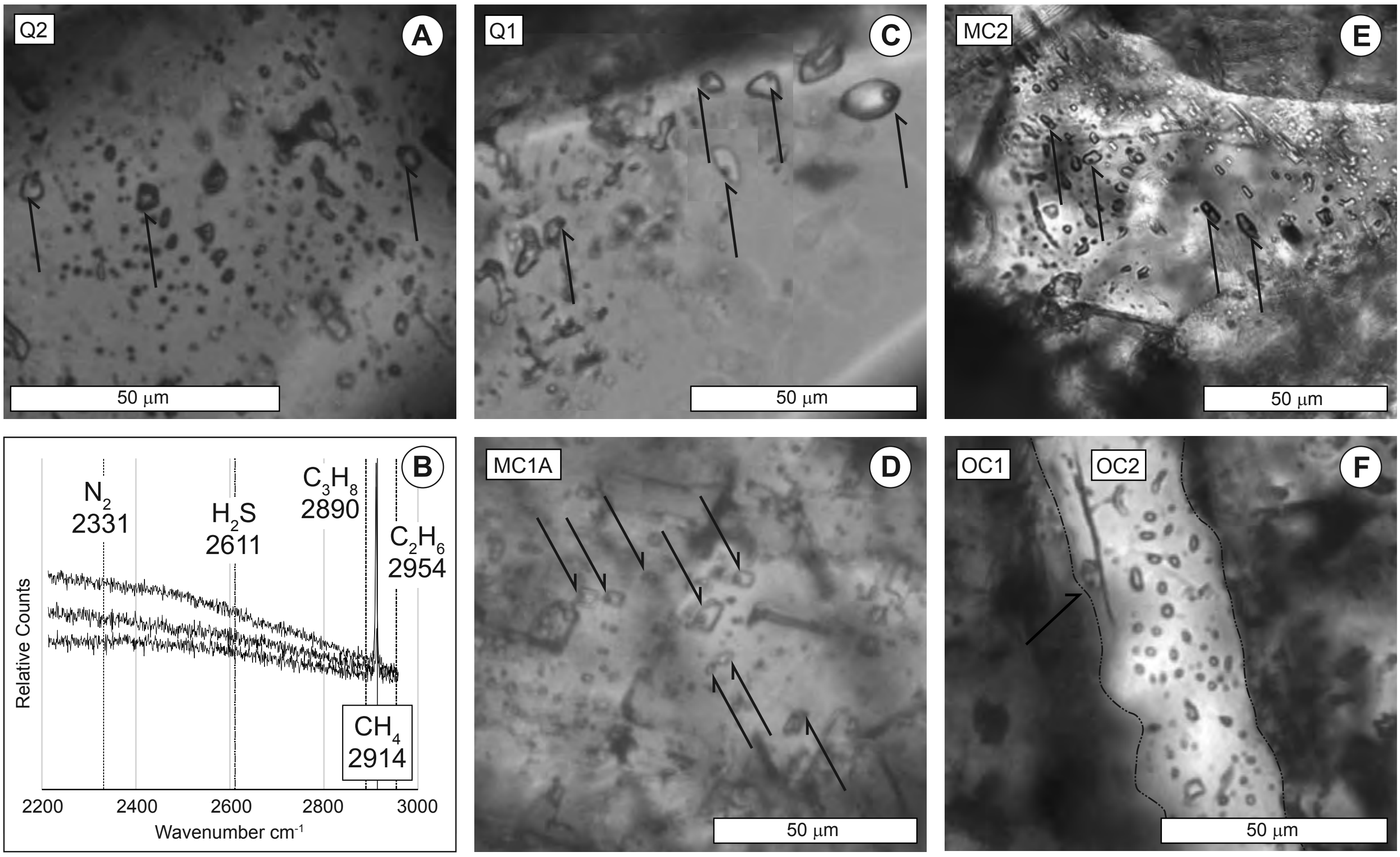

Lucca et al.
Fig. 9

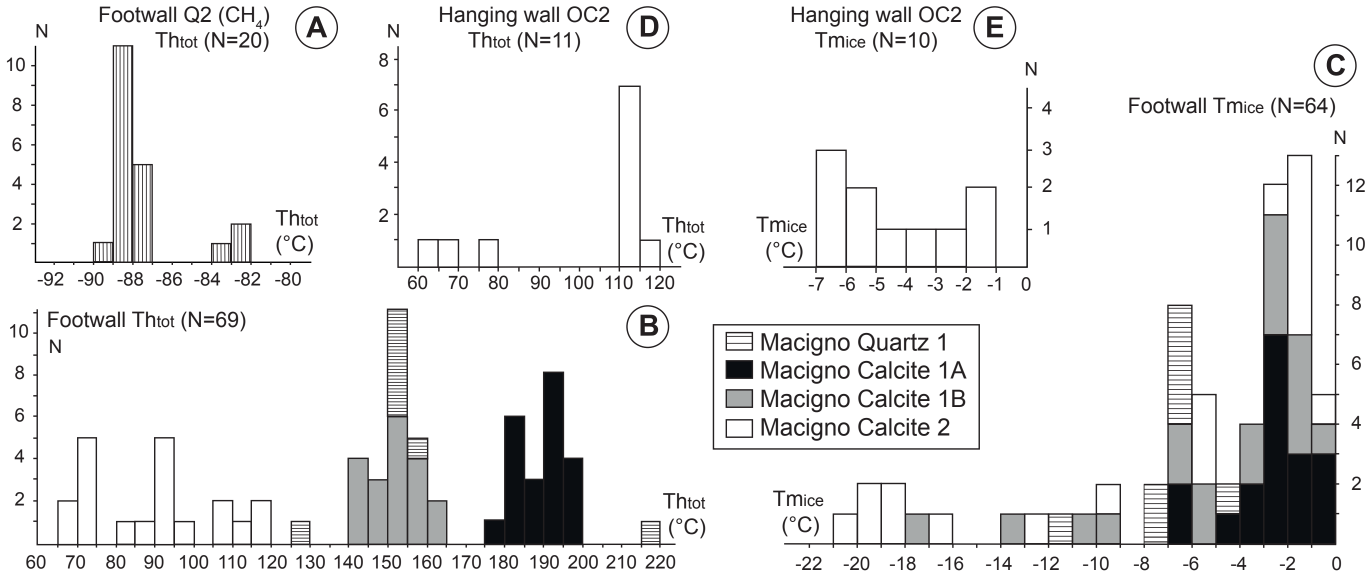

Lucca et al.
Fig. 10

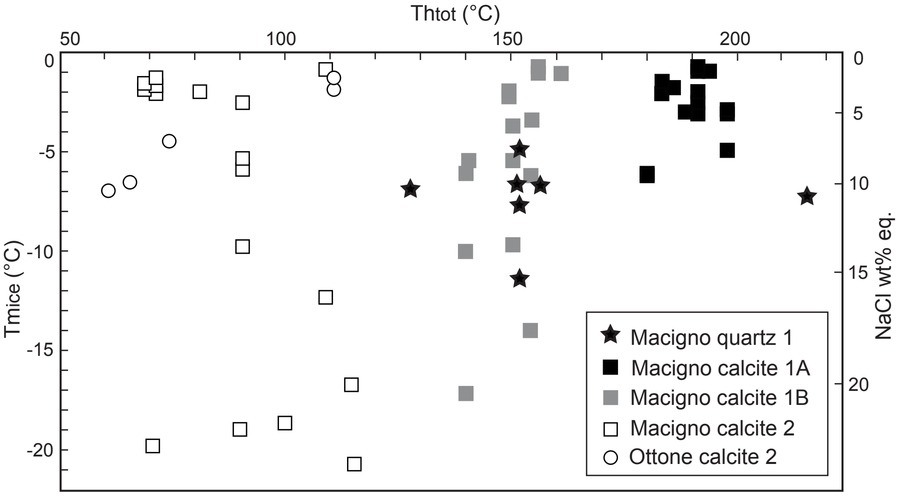

Lucca et al.
Fig. 11

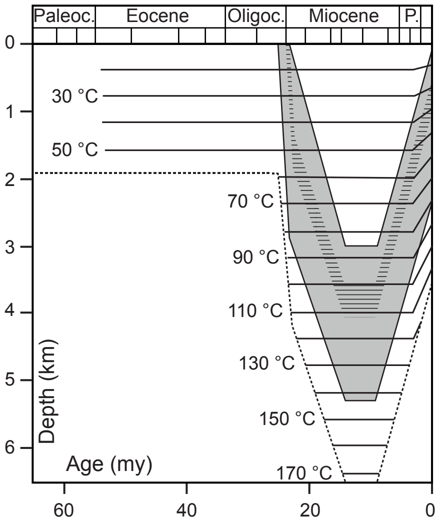

Lucca et al.
Fig. 12

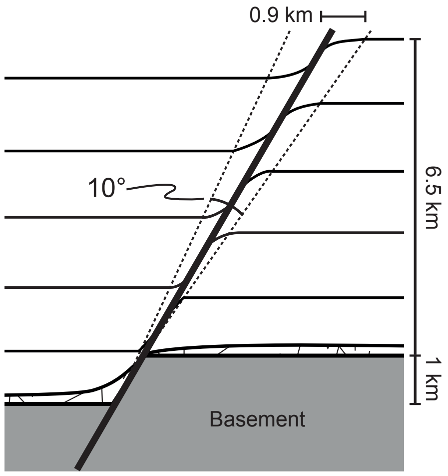

Lucca et al.
Fig. 13

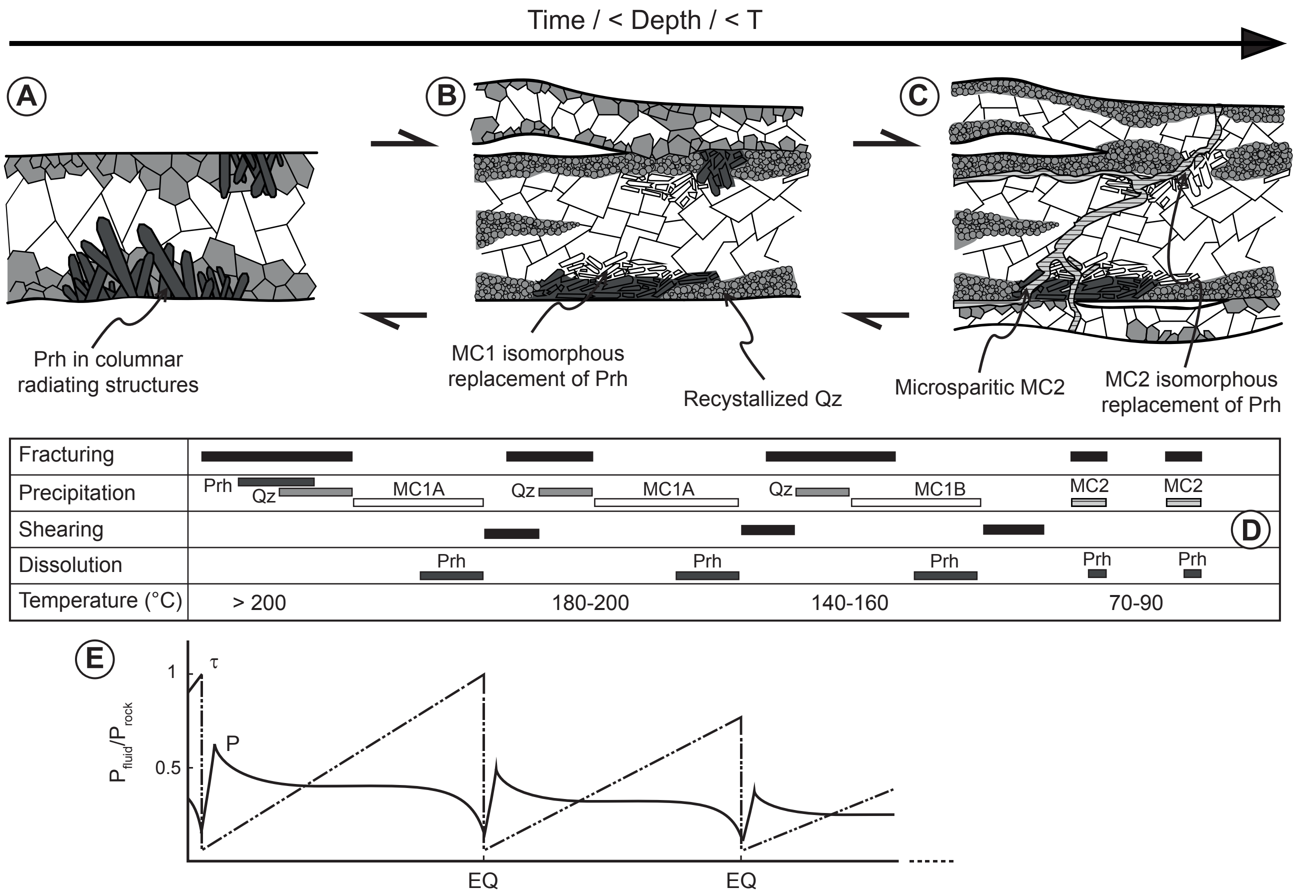

Lucca et al.
Fig. 14

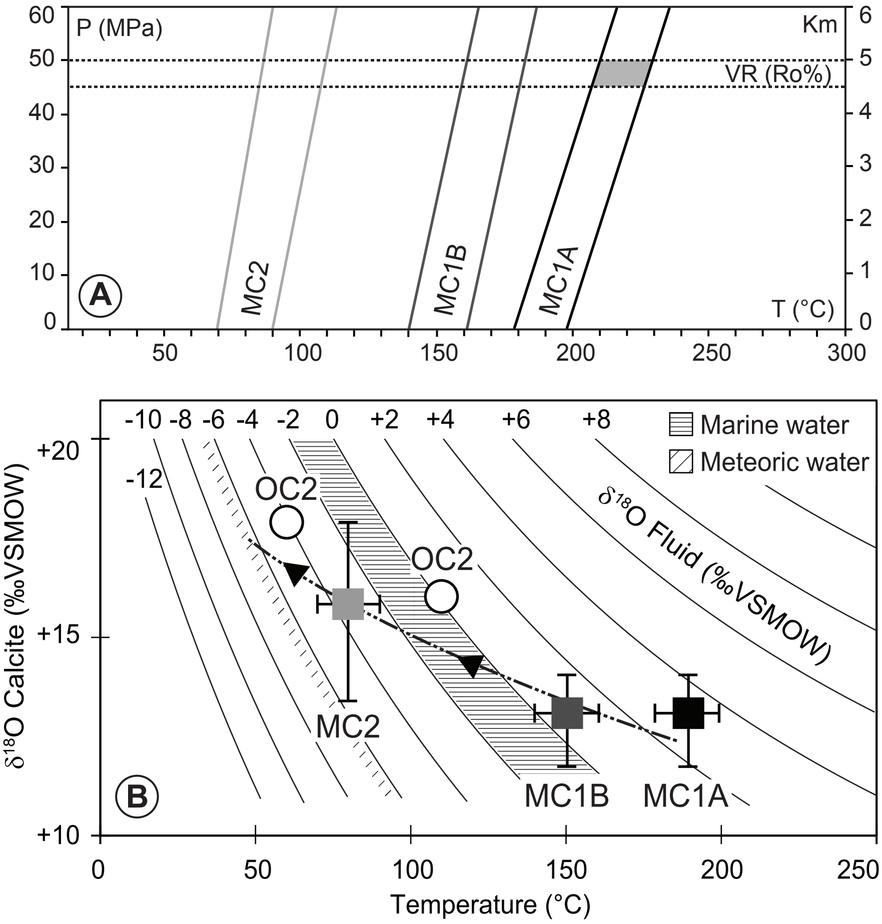

Lucca et al.

Fig. 15

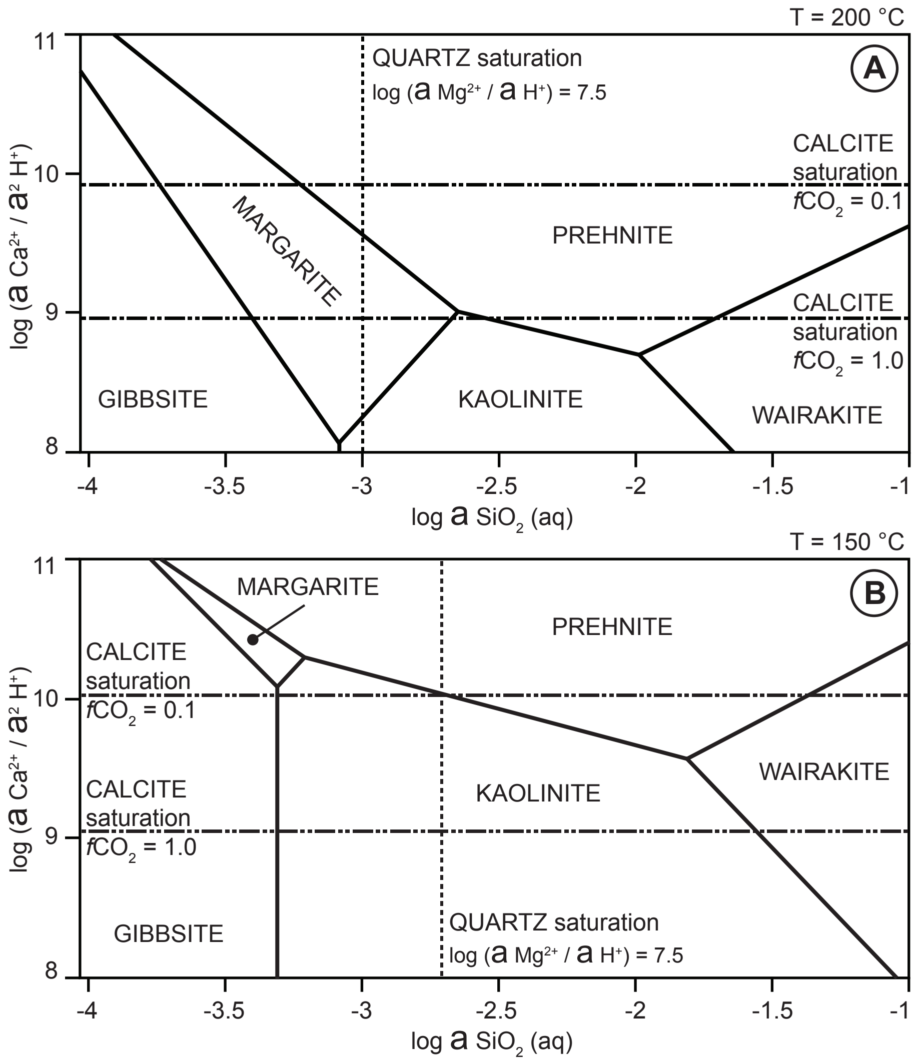

Lucca et al.
Fig. 16

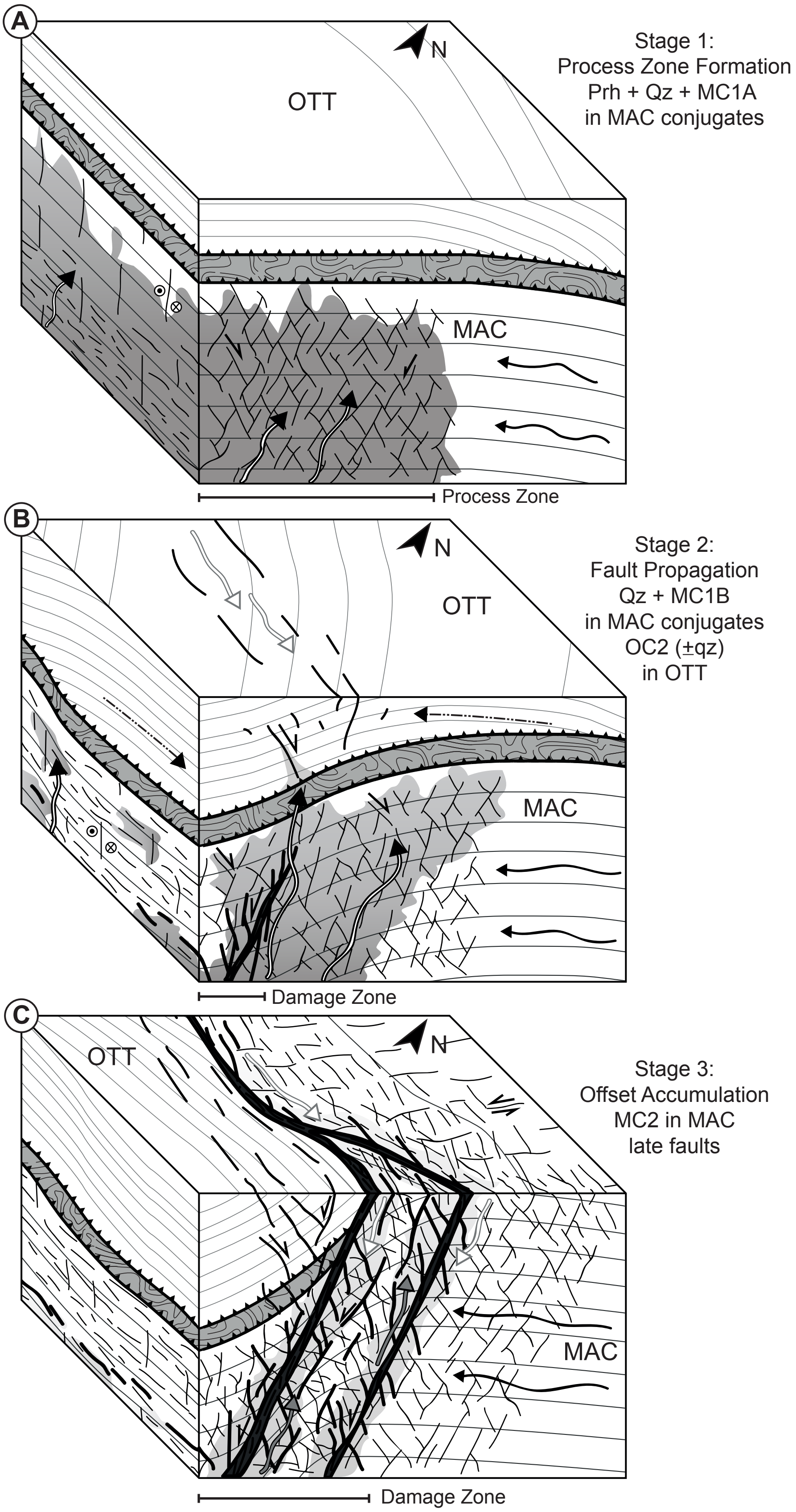

Lucca et al.
Fig. 17

TABLE 1. SUMMARY OF PETROGRAPHIC OBSERVATIONS AND STABLE ISOTOPES ANALYSIS RESULTS OF THE DIFFERENT CARBONATE CEMENTS

Cement	Texture description	$\delta^{18}O$ ‰ (V-SMOW) range	$\delta^{18}O$ ‰ (V-SMOW) mean	$\delta^{18}O$ ‰ (V-SMOW) st. dev.	$\delta^{13}C$ ‰ (V-PDB) range	$\delta^{13}C$ ‰ (V-PDB) mean	$\delta^{13}C$ ‰ (V-PDB) st. dev.
Ottone host rock (n=4)	Anhedral calcite microcrystals in matrix; Non luminescent in clay-silt size beds; dull luminescent in silt-fine sands beds.	+ 26.9 to + 27.5	+ 27.2	± 0.2	+ 1.7 to + 2.0	+ 1.9	± 0.1
Ottone calcite 1 (n=26)	Well developed, rhomboedric “dirty” crystals with abundant twinning Type I, undulose extinction, intercrystalline slip and dissolution surfaces; non to dull luminscence.	+ 23.5 to + 26.9	+ 25.7	± 0.7	+ 1.6 to + 2.4	+ 1.9	± 0.2
Ottone calcite 2 (n=16)	Clean translucent crystals in late fractures with rare twinning Type I; non to dull luminscence.	+ 13.1 to + 19.7	+ 16.5	± 1.6	- 0.5 to + 2.2	+ 1.8	± 0.7
Macigno host rock (n=3)	Anhedral calcite microcrystals in matrix of fine clay-silt beds; red to orange luminescence.	+ 13.9 to + 16.0	+ 14.7	± 1.1	- 3.2 to - 0.7	- 2.1	± 1.3
Macigno calcite 1 (n=21)	Crystals characterized by twinning Type I and rare Type II, displaying rhomboedric and isomorphously replacing Prh; red (MC1A) to orange (MC1B) luminescence.	+ 11.8 to + 14.0	+ 13.1	± 0.6	- 5.8 to - 0.9	- 3.3	± 1.8
Macigno calcite 2 (n=18)	Crystals in late fractures crosscutting Prh, Qz, MC1 and locally replacing Prh; orange to yellow bright luminescence.	+ 13.4 to + 17.9	+ 15.8	± 1.2	- 7.1 to - 0.4	- 2.7	± 2.0

TABLE 2. SUMMARY OF PETROGRAPHIC OBSERVATIONS AND MICROTERMOMETRY ANALYSIS RESULTS OF QUARTZ AND CARBONATE CEMENTS

Cement	FIA origin & type	Homogenization temperature (°C) range/mean	Ice melting temperature (°C) range/mean	Salinity (eq. wt% NaCl) range/mean
Macigno quartz 1	Primary/Pseudosecondary two-phase aqueous	127 to 212 / 157	- 4.8 to - 11.4 / - 7.2	7.6 to 15.4 / 10.7
Macigno quartz 2	Primary Monophase gaseous CH4	- 83 to -89 / -88	N.D.	N.D.
Macigno calcite 1A	Primary/Pseudosecondary two-phase aqueous	178 to 198 / 189	- 0.8 to - 6.2 / -2.7	1.4 to 9.3 / 4.5
Macigno calcite 1B	Primary/Pseudosecondary two-phase aqueous	140 to 161 / 151	- 0.8 to - 17.2 / - 5	1.4 to 20.3 / 7.9
Macigno calcite 2	Primary two-phase aqueous	69 to 115 / 88	- 0.7 to - 20.7 / -8.7	1.2 to 22.9 / 12.5
Ottone calcite 1	Reequilibrated two- and one-phase aqueous	< 50 to 113	0 to - 1.6 / - 0.8	0 to 2.7 / 1.4
Ottone calcite 2	Primary two- and one-phase aqueous	< 50 to 115	- 1.3 to - 6.9 / - 4.4	2.2 to 10.4 / 7

TABLE 3. SUMMARY OF RESULTS OF VITRINITE REFLECTANCE MEASUREMENTS

Site n.	Sample n.	R_0 mean	R_0 S.D.	Data n.
14	1	0.70	0.08	11
14	2	0.66	0.12	8
14	3	0.69	0.10	19
14	4	0.67	0.12	7
4	1	0.61	0.04	8
4	3	0.42	0.06	40
4	4	0.42	0.10	12
5	1	0.46	0.07	29
5	2	0.55	0.05	12
5	3	0.49	0.06	11